actuators

MDPI

Article

Pilot-Opening-Scheduled Gray-Box PWA Identification and Event-Triggered Predictive Control for PWM-Driven Electro-Hydraulic Proportional Valves

Jiazhen Pang, Boqiang Shi *, Hui Guo, Hu Chen and Bingbing Liu

School of Mechanical Engineering, University of Science and Technology Beijing, Beijing 100083, China; m202410441@xs.ustb.edu.cn (J.P.); d202410315@xs.ustb.edu.cn (H.G.); d202310322@xs.ustb.edu.cn (H.C.); m202320634@xs.ustb.edu.cn (B.L.)

* Correspondence: shiboqiang@ustb.edu.cn

Abstract

Predictive control of pulse-width modulation (PWM)-driven electro-hydraulic proportional valves is challenging because PWM commands affect main-spool motion through pilot-spool dynamics and control-chamber pressure build-up. This study develops a compact pilot-opening-scheduled piecewise affine (PWA) predictor that distinguishes command-level PWM hysteresis from the internal pilot-opening modes. A guarded model-selection procedure, termed PhysGuard, compares a warm-start predictor with a bounded-refinement candidate on a short-horizon rollout record that is excluded from fitting and refinement. Under reset-horizon validation, the retained predictor yields displacement root-mean-square errors (RMSEs) of 0.382 mm and 0.596 mm at 80 ms and 120 ms, respectively. The retained predictor is then embedded in a solver-free kinematic dead-zone-crossing-scheduled event-triggered model predictive control (K-DCS-ET-MPC) law. At each complete-search event, the controller evaluates a finite set of pilot-spool references; an inner servo then converts the selected reference into PWM. Over the full 20 s Simulink benchmark, K-DCS-ET-MPC executes 1025 complete finite-set searches, compared with 5001 for time-triggered model predictive control (TT-MPC), giving a 79.5% reduction in search count. Over the common 5–10 s comparison interval, it achieves the lowest mean absolute error (MAE) and RMSE among nine simulated controllers (0.0371 mm and 0.0569 mm). In the same interval, it executes 373 complete searches, compared with 1251 for full-rate kinematic dead-zone-crossing-scheduled model predictive control (K-DCS-MPC), reducing the search count by 70.18%. Linear finite-set model predictive control produces the smallest maximum absolute error. In a nominal bench test with a sinusoidal reference of 5.5 mm amplitude, the MAE and RMSE averaged over three complete cycles are 0.2358 mm and 0.2781 mm, respectively. The robustness results are simulation-based, and complete-search timing is obtained from host-side replay.

Keywords: electro-hydraulic proportional valve; gray-box PWA identification; PWM dead-zone hysteresis; event-triggered predictive control

Check for updates

Academic Editor: Xiaozheng Jin

Received: 23 June 2026
Revised: 23 July 2026
Accepted: 1 August 2026
Published: 6 August 2026

Copyright: © 2026 by the authors. Licensee MDPI, Basel, Switzerland. This article is an open access article distributed under the terms and conditions of the Creative Commons Attribution (CC BY) license.

1. Introduction

Electro-hydraulic proportional and directional valves are widely used in mobile machinery, industrial automation, vehicle actuation, and heavy-duty hydraulic systems because they provide high power density and continuously adjustable flow. Achieving

high-accuracy control of these valves remains challenging because the electrical command affects spool motion through pilot overlap, pressure build-up delay, main-spool friction, directional asymmetry, leakage, and mechanical end stops. Recent studies of proportional-valve systems and pilot-operated proportional directional valves identify valve overlap, pressure–flow coupling, dead-zone compensation, and combined feedforward–feedback disturbance rejection as continuing challenges in electro-hydraulic control [1–5]. Studies of pressure estimation, leakage diagnosis, and braking-by-wire model predictive control (MPC) further show that pressure-state uncertainty and actuator condition are important factors in controlling fluid-power systems [6–8]. Hybrid control of hydraulic directional valves illustrates the potential of combining physics-based and data-driven models [9]. Learning-enhanced predictive control with experimental validation has also been reported for electro-hydraulic track-tensioning systems [10]. Taken together, these studies motivate a computationally bounded predictor that preserves the dominant hydraulic dynamics of the valve's inner loop.

A proportional valve converts an electronic command into metered hydraulic flow between the supply and actuator ports. Consequently, valve pressure drop and leakage, together with sensing bandwidth and embedded implementation constraints, must be considered within the complete hydraulic actuation system [11,12]. Research on pilot-operated directional valves has addressed pilot–main stage coupling, dead-zone compensation, independently controlled pilot stages, micro-flow-based dead-zone detection, and adaptive or intelligent control [13–16]. Glück et al. studied a 4/3 two-stage valve using a control-oriented hybrid model [9]. The present study focuses on the valve's inner loop, with main-spool displacement as the controlled variable because it determines the metering opening. Measured pilot-spool displacement schedules the piecewise affine (PWA) predictor and provides feedback to the inner servo that converts the pilot reference into a pulse-width modulation (PWM) command. The downstream actuator remains outside the prediction model.

The control challenge of a PWM-driven, pilot-operated proportional valve is not adequately represented by a static dead-zone nonlinearity alone. A PWM command first drives the pilot stage, which changes the pilot-orifice openings and the main-spool control-chamber pressures. The resulting pressure difference then generates the hydraulic force that moves the main spool. Thus, command-level hysteresis and the internal pilot-opening modes are related but distinct phenomena. Previous tracking studies have considered dead-zone nonlinearities, adaptive disturbance rejection, and reinforcement learning [17,18]. Data-driven nonlinear MPC for heavy-load hydraulic robots has also shown the potential of multistep learned prediction in hydraulic systems [19]. A controller intended for embedded deployment therefore requires a computationally bounded model that preserves the pilot-to-pressure-to-main spool cascade while distinguishing measured PWM hysteresis from the internal switching surfaces.

A controller-oriented predictor should remain bounded and physically consistent during recursive rollout. Control-oriented identification and data-driven linear-parameter-varying (LPV)/PWA identification studies emphasize that models intended for control should be evaluated on the target task and by their rollout behavior, not solely by one-step fitting accuracy [20–22]. Black-box autoregressive-with-exogenous-input (ARX) and generic PWA models can provide accurate one-step fits but may fail to preserve the physical causal structure during multistep prediction. In contrast, a high-fidelity white-box hydraulic model requires numerous geometric, leakage, and friction parameters that are difficult to identify reliably for embedded use. The proposed gray-box cascaded PWA model balances these requirements by representing the dominant hydraulic channels in a compact affine form. Recent studies of switched-affine identification and PWA predictive con-

trol also support mode-partitioned predictors for systems whose dynamics vary across operating regions [23–27].

Hydraulic MPC and embedded optimal-control tools show that predictive control can be implemented in hydraulic systems and on resource-constrained hardware [28–31]. For the present valve, direct PWM optimization would require the repeated solution of an online problem over a highly switching command-to-motion mapping that includes command hysteresis, pilot motion, pressure build-up, and the main-spool response. A solver-free finite-set law is therefore used instead. A finite set of pilot-reference candidates is propagated through the PWA predictor, an event condition determines when the search is repeated [32–35], and an inner servo converts the selected reference into a PWM command.

To address these issues, this paper makes the following contributions:

1. The method separates macroscopic PWM dead-zone hysteresis from the internal pilot-opening mode partition and schedules the PWA predictor by effective pilot-spool opening rather than PWM amplitude or main-spool displacement.
2. A compact pilot-opening-scheduled PWA predictor is identified. A guarded model-selection procedure, termed PhysGuard, compares a bounded-refinement candidate with the warm-start predictor on a held-out, short-horizon rollout record.
3. The selected predictor is embedded in a solver-free kinematic dead-zone-crossing-scheduled event-triggered model predictive control (K-DCS-ET-MPC) law, in which a finite set of pilot-reference candidates is evaluated through PWA rollout. The selected reference is converted into PWM by an inner pilot-spool servo with actuator limits. This formulation avoids an iterative online numerical solver over the strongly hysteretic PWM-to-motion path.
4. The controller is evaluated through closed-loop simulations, sensitivity and prescribed-perturbation studies, controller comparisons, host-side replay, and a nominal-condition bench test. Each evidence source is interpreted within its stated scope.

Table 1 lists the abbreviations used throughout the manuscript.

Table 1. Abbreviations used in the manuscript.

Abbreviation	Meaning	Abbreviation	Meaning
ADC	Analog-to-digital converter	ARX	Autoregressive with exogenous input
CAN	Controller area network	DC	Direct current
DZ-PID	Dead-zone-compensated proportional–integral–derivative control	ET-MPC	Event-triggered model predictive control
FS-MPC	Finite-set model predictive control	FW-ET-MPC	Fixed-weight event-triggered model predictive control
K-DCS	Kinematic dead-zone-crossing scheduling	K-DCS-ET-MPC	Kinematic dead-zone-crossing-scheduled event-triggered model predictive control
K-DCS-MPC	Kinematic dead-zone-crossing-scheduled model predictive control	LPV	Linear-parameter-varying
LVDT	Linear variable differential transformer	MAE	Mean absolute error
MCU	Microcontroller unit	MPC	Model predictive control
OS	Overshoot	PID	Proportional–integral–derivative control
PWA	Piecewise affine	PWM	Pulse-width modulation
RMSE	Root-mean-square error	SMC	Sliding mode control
TT-MPC	Time-triggered model predictive control		

2. Valve Mechanism and Experimental Dead-Zone Characterization

2.1. Cascade Fluid-Power Mechanism

The investigated plant is a pilot-operated electro-hydraulic proportional directional valve. The pilot stage regulates the main-spool control-chamber pressures instead of transmitting mechanical displacement directly to the main spool. Figure 1 shows the hydraulic test bench and the control and data-acquisition boundary used in this study. The hydraulic subsystem contains the pump, load branches, load valves, and pilot-operated proportional directional valve. The controller, controller area network (CAN) analyzer, host computer, and 12 V direct-current (DC) supply form the external control and logging subsystem. Figure 2 shows the internal valve structure. When the pilot spool moves beyond the positive overlap boundary, one main-spool control chamber is connected to the supply line, and the other is relieved. Reversing the pilot opening reverses the pressure difference. Within the overlap region, the effective pilot-flow area is approximately zero, and the chamber pressure difference cannot be sustained.

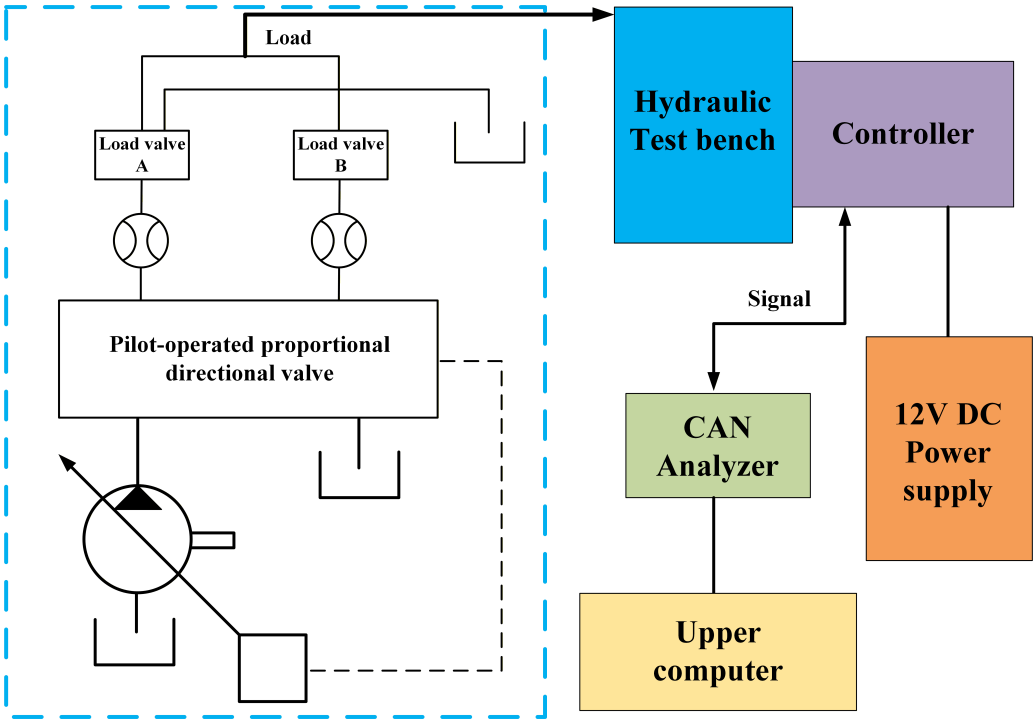


Figure 1. System boundary of the hydraulic test bench. The blue dashed outline encloses the hydraulic plant; colored blocks denote the external test-bench, control, power-supply, and logging components. Black hydraulic symbols and solid connectors show the fluid-power circuit, while arrows indicate signal or information flow.

The valve lies between the hydraulic supply and the actuator ports of a load-sensing multi-way valve system. The investigated assembly comprises a positively overlapped 4/3 pilot spool valve, a main valve with shaped metering grooves, a pressure compensator, return springs, and an onboard controller. The positive pilot overlap reduces internal leakage but creates a near-neutral dead zone. Once the pilot opening exceeds the overlap, the pilot stage directs oil to one main-spool control chamber and relieves the other; the resulting pressure difference moves the larger main spool. This hydraulic amplification is the reason for the two-stage arrangement.

The pressure compensator is located upstream of the main metering spool and maintains an approximately constant pressure drop across the metering edges. The main-spool

opening regulates the working-port flow delivered to the downstream load, while an outer controller may regulate actuator velocity, force, or displacement.

Figure 1 defines the scope of the valve inner-loop study. The hydraulic components lie within the plant boundary, whereas the controller and logging hardware form the external control and data-acquisition subsystem. Figure 2 details the internal pilot–main valve cascade.

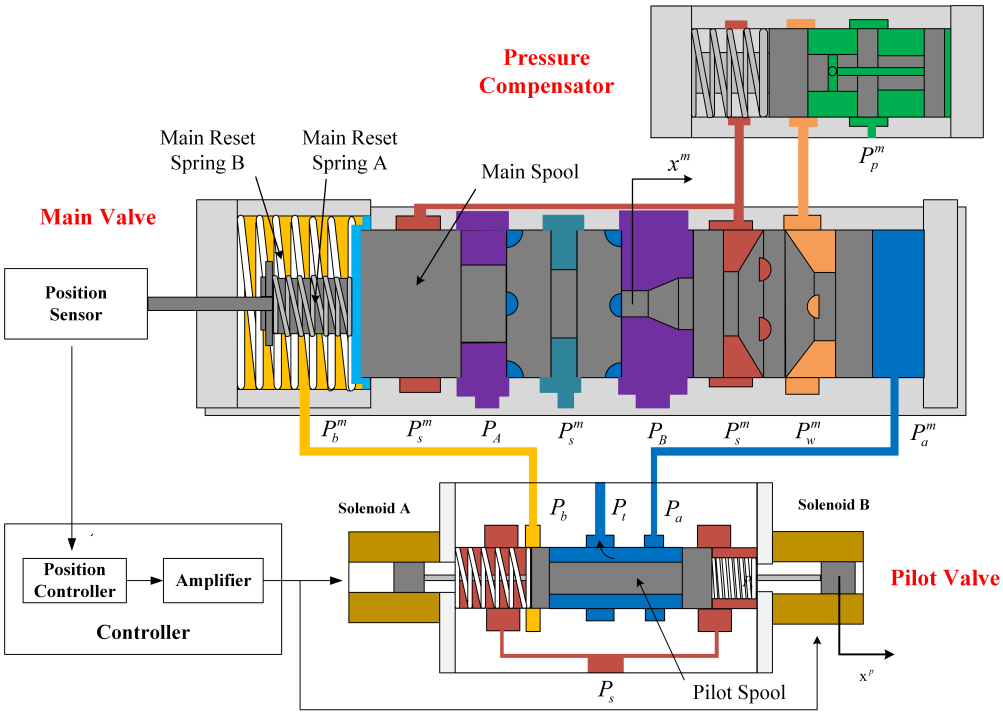


Figure 2. PWM-driven pilot-to-main spool cascade inside the proportional directional valve. Pilot opening changes the control-chamber pressures before the main-spool response develops.

The reduced model follows the cascade expressed as

$$u_k \rightarrow x_{p,k} \rightarrow x_{p,\mathrm{eff},k} \rightarrow (p_{a,k}, p_{b,k}) \rightarrow \Delta p_k \rightarrow v_{m,k} \rightarrow x_{m,k}, \tag{1}$$

Here, u_k is the PWM command, $x_{p,k}$ is the pilot-spool displacement, and $x_{p,\mathrm{eff},k}$ is the signed effective pilot opening after overlap compensation. The $p_{a,k}$ and $p_{b,k}$ variables are the chamber pressures, $\Delta p_k = p_{b,k} - p_{a,k}$ is the driving pressure difference, and $x_{m,k}$ and $v_{m,k}$ are the main-spool displacement and velocity, respectively.

At the system level, $x_{m,k}$ determines the metering area and the working-port flows (Q_A and Q_B), which drive the downstream actuator. The compact predictor ends at x_m; the actuator and load remain outside the valve inner-loop model.

The nominal simulation uses an oil temperature of 45 °C and a main-system supply pressure of 20 MPa. The reduced model assumes an oil density of 850 kg/m^3, a nominal kinematic viscosity of 4.6×10^{-5} m^2/s, a 20 bar pilot supply, and a 200 bar relief setting. The physical test bench uses No. 46 anti-wear hydraulic oil at 45 ± 5 °C, with a 20 MPa main-system supply and a 10 MPa load pressure. Because the return line is connected to the tank, its nominal pressure is taken as 0 MPa gauge. The pilot supply, main-system supply, and return pressures are stated separately because they correspond to different hydraulic boundaries.

The pilot- and main-spool masses used in the reduced model are 0.02 and 0.2 kg, respectively. The pilot-spool diameter is 6 mm, the pilot metering-orifice diameter is 2 mm, and the main-spool diameter is 18 mm. In the presently identified predictor, both

the identified pilot-overlap threshold and the controller-side pilot-overlap threshold are 0.52 mm, and main-spool displacement is constrained to [−10.56, 7.07] mm.

The overlap and dead-zone values are nominal calibrations for this valve and operating envelope. Temperature, pressure, spool wear, and contamination can shift the apparent motion-onset thresholds. Practical deployment requires calibration of $x_{p,\mathrm{dz}}$ and the PWM thresholds during commissioning, followed by recalibration or scheduling if the operating conditions change substantially.

2.2. Control-Oriented Modeling Rationale

The reduced model is designed for controller prediction, not for unique identification of the parameters of every hydraulic component. The reduced relations preserve the dominant causal paths and sign conventions used in the discrete predictor.

Pilot-spool displacement determines whether the pilot-metering ports are effectively open:

$$A(x_p) = \begin{cases} \bar{A}(x_p - x_{p,\mathrm{dz}}), & x_p > x_{p,\mathrm{dz}}, \\ 0, & |x_p| \le x_{p,\mathrm{dz}}, \\ -\bar{A}(-x_p - x_{p,\mathrm{dz}}), & x_p < -x_{p,\mathrm{dz}}, \end{cases} \tag{2}$$

where $\bar{A}(\cdot)$ is a monotone reduced opening map. Here, $A(x_p)$ denotes the signed effective pilot-orifice area, whereas $x_{p,\mathrm{eff}}$ in (9) is the reduced signed opening displacement used by the compact predictor. The nonlinear orifice-area curve is not identified separately; its local relationship with the overlap-compensated pilot displacement is captured by the affine branch gains applied to $x_{p,\mathrm{eff}}$. This map motivates the use of pilot opening, instead of raw PWM or main-spool displacement, as the internal PWA switching variable. The incremental pressure model in (11) and (12) provides reduced representations of the pilot-orifice law and chamber continuity equations. Leakage is represented by relaxation toward P_{bal}, and the constant pressure-bias term is omitted to avoid drift.

The main-spool branch keeps only the force-balance structure needed by the controller-facing predictor, i.e.,

$$m_m \frac{d^2 x_m}{dt^2} \approx A_b p_b - A_a p_a - b_m \frac{dx_m}{dt} - f_s(x_m) - f_r, \tag{3}$$

where m_m is the main-spool mass, dx_m/dt and d^2x_m/dt^2 are the main-spool velocity and acceleration, A_a and A_b are the effective chamber areas, b_m is the viscous damping coefficient, and $f_s(x_m)$ is the spring and end-stop restoring force. The residual term (f_r) combines direction-dependent friction with unmodeled flow-force effects. When the two chamber areas are assumed to be equal, the reduced predictor represents the pressure force through the signed pressure difference. This approximation leads to the effective-opening-driven affine motion law introduced below. The identification diagnostics are reported in equivalent-velocity form, whereas the final controller-oriented predictor stores the displacement increment per sample. Although lower in order than a full hydraulic model, the reduced predictor retains the dominant physical channels required for recursive ET-MPC prediction.

2.3. Triangular Sweep for Macroscopic PWM Dead-Zone Hysteresis

The triangular sweep characterizes the macroscopic relationship between the electrical command and the measured main-spool motion. It provides a command-side interpretation of the dead zone and hysteresis but does not define the internal PWA mode partition. The command follows the sequence expressed as

$$0 \rightarrow +100\% \rightarrow 0 \rightarrow -100\% \rightarrow 0, \tag{4}$$

with a 50 s interval for each segment. Figure 3 shows the full triangular command and displacement response. Figure 4 separates the branchwise onset traces, PWM–displacement loops, and detected motion thresholds. The detected thresholds are summarized as

$$\begin{aligned} u^{+}_{\text{open}} &= 37.728\%, \quad & u^{+}_{\text{close}} &= 33.968\%, \\ u^{-}_{\text{open}} &= -37.464\%, \quad & u^{-}_{\text{close}} &= -34.072\%. \end{aligned} \tag{5}$$

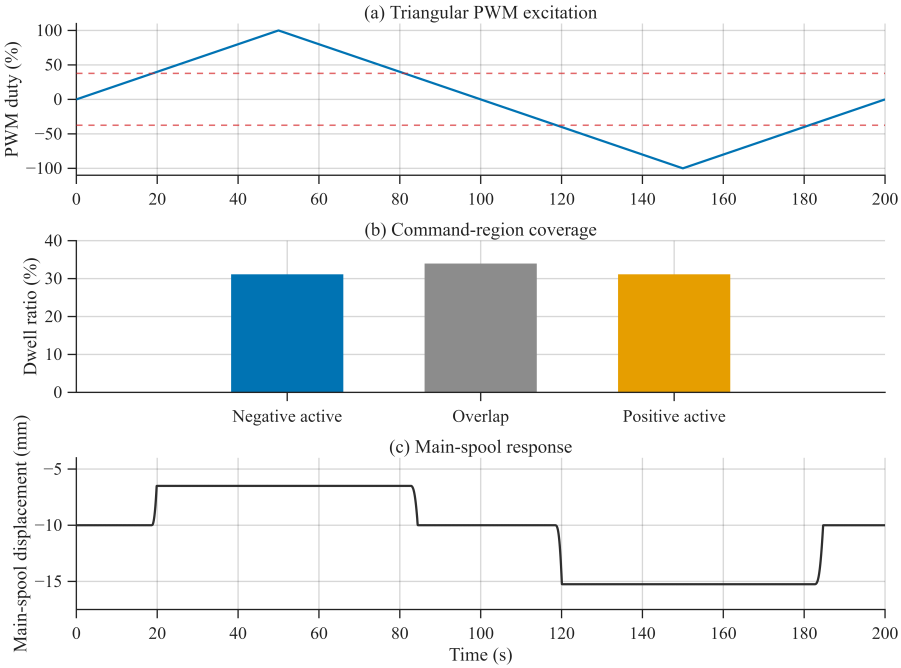


Figure 3. Triangular PWM sweep used to expose command-level dead-zone hysteresis and the delayed onset of measurable main-spool motion. In (**a**), the solid blue line is the commanded PWM sweep and the red dashed lines mark the detected positive and negative opening thresholds. In (**b**), blue, gray, and orange bars denote the negative-active, overlap, and positive-active command regions, respectively. The dark gray line in (**c**) is the measured main-spool displacement.

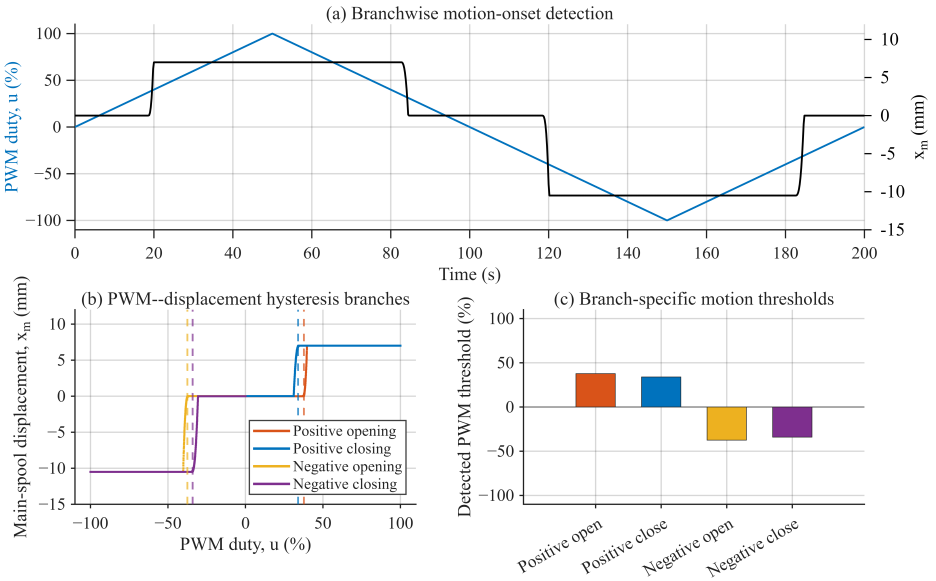


Figure 4. Branchwise PWM onset thresholds and displacement hysteresis used for command-side calibration. In (**a**), the blue and black solid lines are PWM duty and main-spool displacement.

In (**b**), orange, blue, yellow, and purple identify positive opening, positive closing, negative opening, and negative closing, respectively; the matching dashed vertical lines mark their detected PWM thresholds. Panel (**c**) summarizes the same four thresholds.

The larger opening magnitudes relative to the corresponding closing magnitudes indicate command-level hysteresis. This behavior can arise from pilot overlap, stiction, chamber pressure build-up, and spring preload, although the sweep does not identify their individual contributions. These thresholds characterize the assembled hydraulic system and are not used as internal PWA switching surfaces. Because they may vary with temperature, pressure, and valve condition, they should be verified during commissioning.

3. Pilot-Opening-Based Cascade Gray-Box PWA Model

The modeling framework has two linked levels. The pressure-channel equations support physical interpretation and diagnostics, whereas the compact displacement-increment predictor is used for online rollout. This predictor uses three affine regions corresponding to positive pilot opening, the overlap/dead zone, and the negative pilot opening. A single affine model would conflate both pressure build-up directions with the centered overlap behavior. However, the available transition data are insufficient to support a finer partition. The resulting three-region structure captures the observed switching behavior without introducing poorly supported modes.

3.1. Pilot Dynamics and Effective Opening

The pilot-stage motion is approximated by a direction-dependent first-order affine discrete model:

$$x_{p,k+1} = a_p^{(s)} x_{p,k} + b_p^{(s)} u_k + c_p^{(s)}, \qquad s \in \{+, -\}. \tag{6}$$

The sign of the applied PWM command selects the branch index: $s = +$ for $u_k \geq 0$ and $s = -$ for $u_k < 0$. Section 5 introduces the PWM synthesis relation used by the final controller. The final selected constants, obtained using the guarded procedure described in Section 4.3, are

$$[a_p^{(+)}, b_p^{(+)}, c_p^{(+)}] = [0.946965,\ 7.32084 \times 10^{-4},\ 1.14651 \times 10^{-4}], \tag{7}$$

$$[a_p^{(-)}, b_p^{(-)}, c_p^{(-)}] = [0.946650,\ 7.34633 \times 10^{-4},\ -2.31205 \times 10^{-4}]. \tag{8}$$

The effective pilot opening is defined by an overlap compensation map:

$$x_{p,\mathrm{eff},k} = \begin{cases} x_{p,k} - x_{p,\mathrm{dz}}, & x_{p,k} > x_{p,\mathrm{dz}}, \\ 0, & |x_{p,k}| \leq x_{p,\mathrm{dz}}, \\ x_{p,k} + x_{p,\mathrm{dz}}, & x_{p,k} < -x_{p,\mathrm{dz}}, \end{cases} \qquad x_{p,\mathrm{dz}} = 0.52 \text{ mm}. \tag{9}$$

The corresponding three modes are

$$\mathcal{M}(x_{p,k}) = \begin{cases} 1 \text{ (Pilot_PosOpen)}, & x_{p,k} > +0.52 \text{ mm}, \\ 2 \text{ (Pilot_OverlapDeadzone)}, & |x_{p,k}| \leq 0.52 \text{ mm}, \\ 3 \text{ (Pilot_NegOpen)}, & x_{p,k} < -0.52 \text{ mm}. \end{cases} \tag{10}$$

Figure 5 shows representative positive- and negative-opening segments and illustrates both the mode partition and the signed effective opening.

The zero plateaus of $x_{p,\mathrm{eff}}$ in Figure 5 motivate the modeling of the overlap branch as a damped, centered, dynamic mode rather than a static, zero-motion state. The controller-oriented predictor therefore switches according to the measured pilot open-

ing instead of the raw PWM command. The threshold of $x_{p,\mathrm{dz}} = 0.52$ mm is the nominal identified overlap for the tested valve. Small transition mismatches near ±0.52 mm are expected because pilot motion, pressure build-up, friction, and sampling are not instantaneous. The model retains a separate overlap branch and treats transition-point errors as secondary diagnostics.

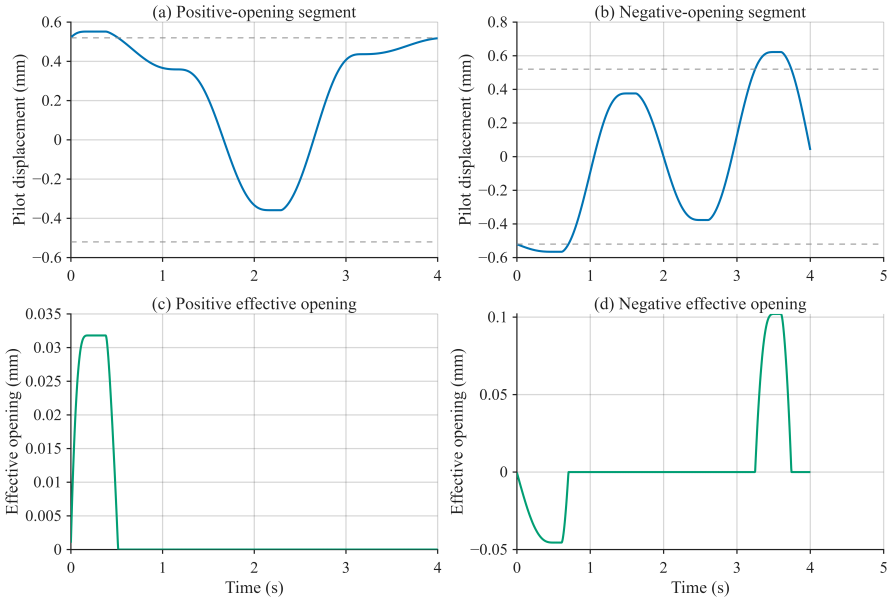


Figure 5. Pilot-opening mode partition and overlap-compensated signed effective opening. The three regions correspond to positive opening, overlap, and negative opening. Blue solid lines show measured pilot-spool displacement, gray dashed lines mark the ±0.52 mm overlap boundaries, and green solid lines show the resulting signed effective opening.

3.2. Incremental Pressure Build-Up and Leakage Model

The chamber-pressure dynamics are represented by incremental equations that include leakage toward a balance pressure (P_{bal}). A constant pressure-bias term is omitted to prevent non-physical drift when the effective pilot opening is zero. In (11)–(15), $x^{(\mathrm{m})}_{p,\mathrm{eff},k} = 10^{-3} x_{p,\mathrm{eff},k}$ is expressed in meters to maintain unit consistency in the pressure channels. The diagnostic equations express velocity in mm/s and pressure in bar, whereas the compact predictor in (17)–(19) uses displacement in millimeters. The fitted coefficients incorporate these empirical unit conversions and the sampling interval. They are therefore interpreted as control-oriented gains rather than component-level hydraulic parameters:

$$\Delta p_{a,k} = \alpha_{a,1} v_{m,k} + \alpha_{a,2} x^{(\mathrm{m})}_{p,\mathrm{eff},k} + \alpha_{a,3}(P_{\mathrm{bal}} - p_{a,k}), \tag{11}$$

$$\Delta p_{b,k} = \alpha_{b,1} v_{m,k} + \alpha_{b,2} x^{(\mathrm{m})}_{p,\mathrm{eff},k} + \alpha_{b,3}(P_{\mathrm{bal}} - p_{b,k}). \tag{12}$$

The absolute pressures are updated by

$$\begin{aligned} p_{a,k+1} &= \mathrm{sat}_{[P_t,P_s]}\left(p_{a,k} + \Delta p_{a,k}\right), \\ p_{b,k+1} &= \mathrm{sat}_{[P_t,P_s]}\left(p_{b,k} + \Delta p_{b,k}\right), \end{aligned} \tag{13}$$

where $P_s = 20.16$ bar and $P_t = -0.9516$ bar are the identified control-chamber pressure bounds, $P_{\mathrm{bal}} = -0.9516$ bar, and $\mathrm{sat}_{[P_t,P_s]}(z) = \min(\max(z, P_t), P_s)$. The upper bound ($P_s$) is distinct from both the 20 bar pilot supply and the 20 MPa main-system supply. The lower bound (P_t) is data-calibrated and includes the measurement zero offset; it is not the physical return-line set point. The nominal tank-connected return boundary is 0 MPa gauge.

The identified pressure parameters are

$$\Delta p_{a,k} = 8.228 \times 10^{-9} v_{m,k} - 942.9583 x^{(\mathrm{m})}_{p,\mathrm{eff},k} + 0.0111(P_{\mathrm{bal}} - p_{a,k}), \tag{14}$$

$$\Delta p_{b,k} = -8.634 \times 10^{-9} v_{m,k} + 1133.3874 x^{(\mathrm{m})}_{p,\mathrm{eff},k} + 0.0106(P_{\mathrm{bal}} - p_{b,k}). \tag{15}$$

The signs of the effective-opening gains are consistent with the observed cascade: positive effective opening lowers one chamber pressure and raises the other, whereas negative effective opening reverses the pressure difference. The *A*- and *B*-chamber coefficients are lumped, control-oriented gains. They capture asymmetric pilot passages, local pressure losses, directional flow forces, friction, and residual identification error after the reduction of the continuity equations. They preserve the measured pressure-difference trend rather than identifying each physical chamber parameter separately.

3.3. Main-Spool PWA Increment Dynamics

To reduce the online state dimension, the model represents the pressure build-up dynamics through a displacement-increment equation driven by the effective pilot opening. Except in the pressure-channel diagnostic Equations (11)–(15), Sections 3 and 4 express x_p and x_m in millimeters, the diagnostic velocity (v_m) in mm/s, pressure in bar, and u_k as a PWM duty percentage. The low-complexity ET-MPC predictor stores x_m, x_p, and the per-sample displacement increment (Δx_m) in millimeters. The centering term is based on the normalized main-spool displacement, i.e.,

$$x_{n,k} = \frac{x_{m,k} - x_{\mathrm{eq}}}{x_{\mathrm{scale}}}, \qquad x_{\mathrm{eq}} = 0, \quad x_{\mathrm{scale}} = 10.620 \text{ mm}, \tag{16}$$

which is the same scaling used by the controller implementation:

$$\Delta x_{m,k+1} = a^{(i)}_{\Delta} \Delta x_{m,k} + b^{(i)}_{x} x_{p,\mathrm{eff},k} + k^{(i)}_{x} x_{n,k} + c^{(i)}. \tag{17}$$

Here, $a^{(i)}_{\Delta}$ represents discrete increment memory, $b^{(i)}_{x}$ is the effective-opening drive gain, $k^{(i)}_{x}$ is the local centering term, and $c^{(i)}$ is the residual branch offset retained by the compact predictor. For the overlap dead-zone mode, effective-opening drive is disabled:

$$\Delta x_{m,k+1} = a^{(2)}_{\Delta} \Delta x_{m,k} + k^{(2)}_{x} x_{n,k} + c^{(2)}. \tag{18}$$

The main-spool displacement is updated directly by the predicted increment:

$$x_{m,k+1} = x_{m,k} + \Delta x_{m,k+1}. \tag{19}$$

The final selected main-spool constants are listed in Table 2. Section 4.3 describes the guarded selection procedure, while Section 4.2 reports the associated regression-row counts.

Table 2. Selected constants of the main-spool displacement-increment submodel.

Mode	Region	a_{Δ}	b_x	k_x	c
M1	Positive opening	0.7500	0.8000	−0.01383	−0.001493
M2	Overlap dead zone	0.91136	0	−0.002085	4.1969×10^{-5}
M3	Negative opening	0.7500	0.80003	−0.01169	0.001281

Note: k_x multiplies the normalized main-spool displacement (x_n) in (16).

The two active modes retain comparable effective-opening gains and negative centering terms, while the overlap mode removes the opening-drive channel and is dominated

by increment decay and the centering effect. Accordingly, these coefficients are interpreted as control-oriented effective constants rather than unique component parameters.

Figure 6 summarizes the physical consistency of the reduced predictor across the cascade from pilot opening to chamber pressure and main-spool motion. The positive- and negative-opening segments show that the predictor preserves the sequence of pressure build-up, signed main-spool velocity, and displacement. The figure provides a mechanistic consistency check, not a closed-loop tracking result. The positive and negative responses are not mirror-symmetric because the two flow paths have different metering edges and chamber passages, and the spool has direction-dependent friction and flow-force effects. The predictor preserves this measured asymmetry instead of imposing identical branch coefficients.

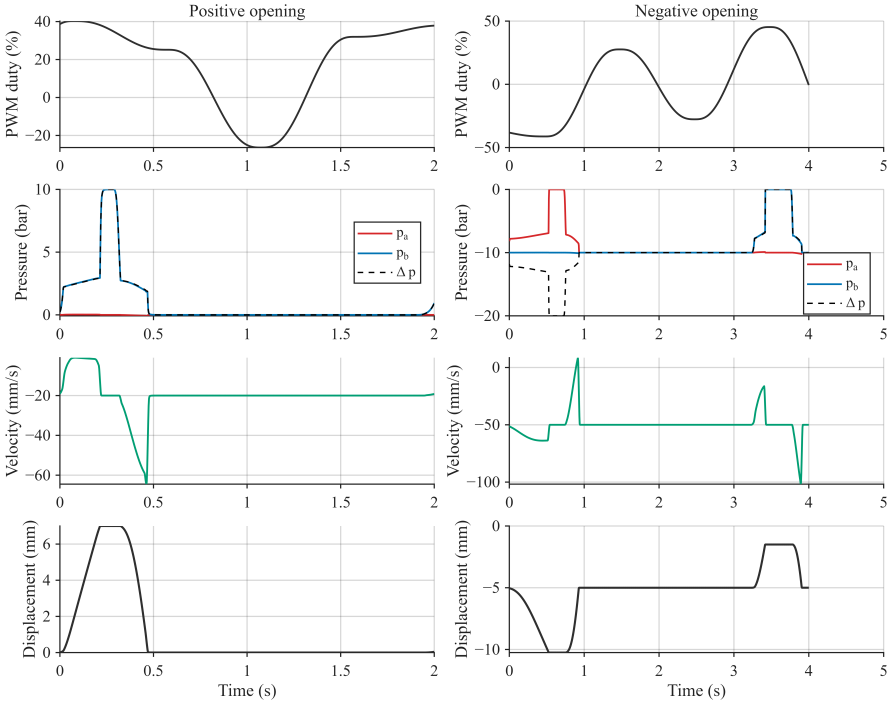


Figure 6. Representative hydraulic cascade response. Changes in pilot opening precede the chamber-pressure, main-spool velocity, and displacement responses. In the pressure panels, red and blue solid lines denote p_a and p_b, and the black dashed line denotes $\Delta p = p_b - p_a$; green and dark gray solid lines denote main-spool velocity and displacement in the lower panels.

4. Identification Procedure and Validation Results

4.1. Constrained Gray-Box Identification Theory

Each subsystem is identified as a constrained regression problem derived from the physical variables in Section 3. For a generic branch, the measured target (y) and regressor matrix (Φ) satisfy

$$y = \Phi\theta + \varepsilon, \tag{20}$$

where θ is the parameter vector and ε represents measurement noise, unmodeled nonlinear flow forces, and residual friction effects. The estimate is obtained by constrained ridge regression:

$$\hat{\theta} = \arg\min_{\theta}\left(\|\Phi\theta - y\|_2^2 + \lambda\|D\theta\|_2^2\right) \quad \text{s.t.} \quad A_{\text{ineq}}\theta \le b_{\text{ineq}}, \quad A_{\text{eq}}\theta = b_{\text{eq}}. \tag{21}$$

The regularization term suppresses ill-conditioned estimates caused by strong correlation between pilot opening, displacement, and local motion states. Here, D is the regularization

scaling matrix. The matrices and vectors (A_{ineq}, b_{ineq}, A_{eq}, and b_{eq}) collect the inequality and equality constraints on coefficient signs, zero structure, and short-horizon rollout bounds. These constraints retain the effective-opening drive channel in the active branches; remove a spurious opening-drive term from the overlap branch; and keep short, recursive rollouts bounded. The fixed ridge weights are $\lambda_p = 10^{-8}$ for the pilot regression, $\lambda_{\Delta p} = 10^{-6}$ for the pressure-increment regressions, and $\lambda_m = 10^{-6}$ for the main-spool regression.

For the pilot stage, the identification target and regressor are

$$y_{p,k} = x_{p,k+1}, \qquad \phi_{p,k} = \begin{bmatrix} x_{p,k} & u_k & 1 \end{bmatrix}, \tag{22}$$

which gives $\theta_p = [a_p, b_p, c_p]^T$. For the pressure channels, the targets are pressure increments, i.e.,

$$y_{a,k} = p_{a,k+1} - p_{a,k}, \qquad y_{b,k} = p_{b,k+1} - p_{b,k}, \tag{23}$$

with regressors expressed as

$$\begin{aligned} \phi_{a,k} &= \begin{bmatrix} v_{m,k} & x^{(m)}_{p,\text{eff},k} & P_{\text{bal}} - p_{a,k} \end{bmatrix}, \\ \phi_{b,k} &= \begin{bmatrix} v_{m,k} & x^{(m)}_{p,\text{eff},k} & P_{\text{bal}} - p_{b,k} \end{bmatrix}. \end{aligned} \tag{24}$$

No constant column is included in (24); otherwise, the pressure model could generate non-physical drift, even when $x_{p,\text{eff}} = 0$.

For the final compact main-spool predictor, the regression target is the per-sample displacement increment ($y_{m,k} = \Delta x_{m,k+1}$). For the active modes ($i \in \{1, 3\}$), the reduced regressor is

$$\phi^{(i)}_{m,k} = \begin{bmatrix} \Delta x_{m,k} & x_{p,\text{eff},k} & x_{n,k} & 1 \end{bmatrix}. \tag{25}$$

For the overlap dead-zone mode, the target remains $\Delta x_{m,k+1}$, but the regressor vector contains only the increment-memory, centering, and constant terms:

$$\phi^{(2)}_{m,k} = \begin{bmatrix} \Delta x_{m,k} & x_{n,k} & 1 \end{bmatrix}, \tag{26}$$

which removes the effective-opening drive term from the dead-zone branch while retaining the small affine offset ($c^{(2)}$) listed in Table 2.

For comparison with conventional motion diagnostics, the one-step parity plot reports the equivalent velocity ($v_{m,k} = \Delta x_{m,k}/T_s$). The one-step validation metric is

$$\text{RMSE}_{v_m} = \sqrt{\frac{1}{N}\sum_{k=1}^{N}\left(v^{\text{pred}}_{m,k} - v^{\text{meas}}_{m,k}\right)^2}, \tag{27}$$

and the recursive rollout drift at horizon h is

$$e_x(h) = \left| x^{\text{pred}}_{m,k+h|k} - x^{\text{meas}}_{m,k+h} \right|. \tag{28}$$

A small one-step residual does not guarantee accurate recursive prediction when the hidden hydraulic dynamics, mode switching, or dead-zone branch is represented inconsistently.

Figures 7 and 8 show the local one-step accuracy, while Figure 9 shows the growth of recursive prediction error. The parity and residual plots use the same equivalent-velocity units. As shown in Figure 9, the mean terminal error substantially exceeds the median because a subset of active-opening transitions accumulates large drift. In closed-loop operation, measurement reinitialization and event-based refreshes limit the influence of this drift. The stroke margins remain safeguards against off-nominal endpoint violations and are inactive along the selected nominal trajectory.

In Figure 7, the sample count (N) in each panel denotes the retained one-step diagnostic samples used for parity visualization. It is not the same as the guarded regression-row count or the pooled modal-coverage count reported in Section 4.2.

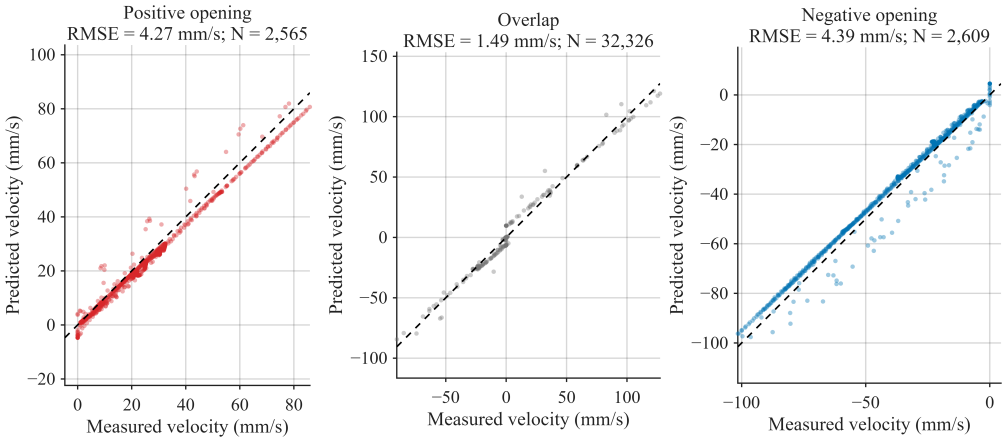


Figure 7. Mode-wise one-step parity in equivalent-velocity units. Red, gray, and blue points denote the positive-opening, overlap, and negative-opening modes, respectively; the black dashed diagonal is the ideal one-to-one line. Each panel shows whether the corresponding affine branch preserves the local signed motion trend required for rollout prediction.

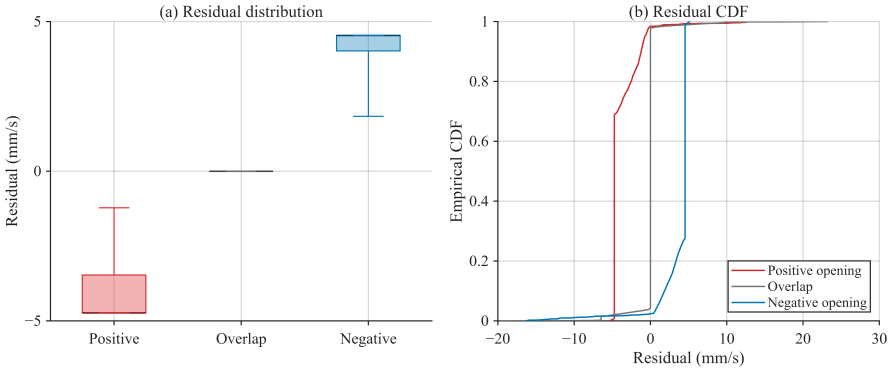


Figure 8. Mode-wise equivalent-velocity residuals. The active-opening branches exhibit broader error distributions than the overlap branch.

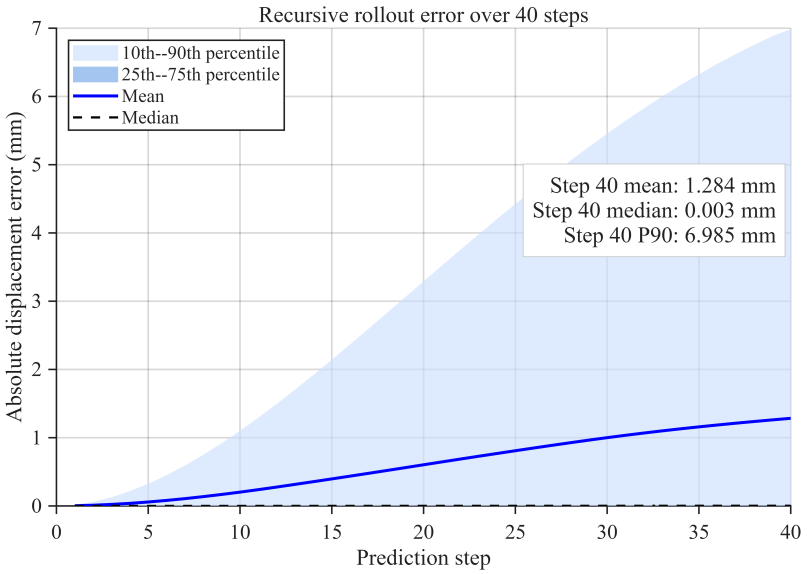


Figure 9. Recursive rollout errors over the 40-step controller prediction horizon.

In Figure 9, the light-blue band spans the 10th–90th percentiles, the darker blue band spans the 25th–75th percentiles, the blue solid line is the mean, and the black dashed line is the median. At step 40, the 25th and 75th percentiles are 0.001606 mm and 0.002807 mm, respectively, whereas the 90th percentile is 6.985314 mm. Consequently, the interquartile band occupies less than 0.02% of the 0–7 mm vertical range and nearly coincides with the median curve; it is therefore not visually distinguishable at the scale of the full-range plot even though it is included in the plotted data.

In closed-loop operation, measurement reinitialization and event-based refreshes limit the influence of this drift. The stroke margins remain safeguards against off-nominal endpoint violations and are inactive along the selected nominal trajectory.

4.2. Data Partition and Modal Coverage

The data processing sequence comprises record collection, 4 ms alignment, filtering, mode assignment, constrained identification, candidate generation, guarded selection, and final validation. The data summary distinguishes record-level sources from the modal coverage of the resulting regression rows. Table 3 lists the records used at each stage. Its raw sample counts refer to complete records before subsampling, delay alignment, segment filtering, and mode assignment. Table 4 reports the modal coverage after these processing and mode-assignment steps.

The identification records contain synchronized PWM, pilot-spool displacement (x_p), main-spool displacement (x_m), chamber pressure, supply and return pressures, and flow measurements sampled at T_s = 4 ms (250 Hz). All identification channels are aligned to this 4 ms grid, which is also used by the controller-oriented discrete predictor. No 1 ms identification or control step is used. For the offline equivalent-velocity diagnostics, the time-ordered main-spool displacement is smoothed with a five-sample moving mean, and its gradient is evaluated at 4 ms intervals. This preprocessing is used only for the identification diagnostics and does not specify the hardware sensor filter.

An additional strict-overlap sensitivity check produced almost exclusively overlap-mode rows. This result indicates that overly conservative thresholding can suppress active-opening transitions. The diagnostic check was not used for final fitting or controller-domain screening.

Figure 10 confirms that both signed active-opening regions are represented in the pooled training data, whereas the guarded screening subset in Table 4 is dominated by overlap samples. Validation reports reset-horizon errors and mode-conditioned one-step errors; transition-point statistics remain secondary because active-opening residuals also include pressure build-up delay, local saturation, flow-force effects, and direction-dependent friction.

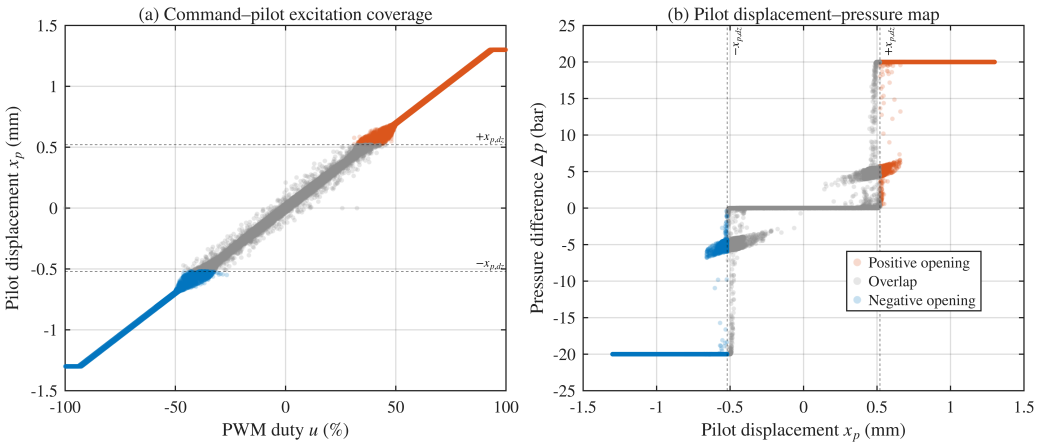


Figure 10. Identification excitation coverage before controller-domain screening, including both signed active-opening regions.

Table 3. Record-level data sources for identification, held-out validation, and control-domain screening.

Data Source	Records	Raw Samples	Role
Broad predictor-fitting pool	Seven training records	262,507	Gray-box regression pool before filtering
Held-out broad validation pool	Two validation records	162,502	Prediction evaluation after alignment and filtering; excluded from fitting
Candidate-generation records	Five command records	–	Bounded-refinement candidate generation
Guarded-selection record	One sinusoidal record	–	Candidate screening and reset-horizon evaluation; excluded from fitting and refinement

Table 4. Regression-row modal coverage for the pilot-opening-scheduled predictor after filtering. M1, M2, and M3 denote positive opening, overlap, and negative opening, respectively.

Row Set	Rows	M1	M2	M3	Interpretation
Broad offset-free search pool	82,766	2363	78,043	2360	Pooled modal data for fitting
Guarded screening subset	15,488	205	15,031	252	Controller-domain screening data; not dense active-opening coverage

4.3. Guarded Short-Rollout Validation

PhysGuard is the guarded model-selection procedure defined by the validation score and acceptance rule below. It compares the warm-start predictor with a bounded-refinement candidate on a held-out, short-rollout record that is not used for fitting or candidate generation. Let θ_0 denote the warm-start constants and θ_c be a candidate returned by bounded control-domain optimization. The corresponding validation score is $S_{\mathcal{V}}^{\mathrm{sel}}(\theta)$. Because the selection, sensitivity, and final-evaluation protocols use different rollout initialization rules, their RMSE values are not compared directly. The final guarded-selection run uses the two reset-horizon RMSE terms stored with the identification result:

$$S_{\mathcal{V}}^{\mathrm{sel}}(\theta) = 0.70\frac{\mathrm{RMSE}_{80}(\theta)}{x_{\mathrm{scale}}} + 0.30\frac{\mathrm{RMSE}_{120}(\theta)}{x_{\mathrm{scale}}}, \qquad x_{\mathrm{scale}} = 10.62\ \mathrm{mm}. \tag{29}$$

The fixed displacement scale and weights are applied to every candidate, so the score is dimensionless and directly reproducible from the unrounded 80 ms and 120 ms RMSE values. Maximum error is not part of this final selection score; it is introduced only in the separate ratio-normalized sensitivity analysis below. The guarded acceptance rule is

$$\theta_{\mathrm{sel}} = \begin{cases} \theta_c, & S_{\mathcal{V}}^{\mathrm{sel}}(\theta_c) < S_{\mathcal{V}}^{\mathrm{sel}}(\theta_0) - \epsilon_g, \\ \theta_0, & \text{otherwise}, \end{cases} \qquad \epsilon_g \geq 0. \tag{30}$$

The warm start is the constrained gray-box predictor before bounded refinement. With $\epsilon_g = 0$, a candidate replaces it only if the held-out validation score is strictly lower. The bounded-refinement candidate reduced the internal refinement objective but increased the held-out validation score. The guarded acceptance rule therefore retained the warm-start predictor, as reported in Table 5 and Figure 11. Here, $\mu = 0$ and $\mu = 1$ denote the warm-start and bounded-refinement predictors, respectively. This notation is used only for guarded predictor selection and is distinct from the ridge-regularization weight (λ) in (21).

Table 5 reports the final PhysGuard selection score. Tables 6 and 7 use a dense multi-origin sensitivity protocol based on a sinusoidal PWM record with an amplitude of 60%. The record contains PWM, pilot-spool displacement (x_p), and main-spool displacement (x_m). At each valid rollout origin, the measured x_p selects the PWA mode, and the rollout is reinitialized from the measured x_m every five samples. At $T_s = 4$ ms, the 20- and 30-sample horizons correspond to 80 and 120 ms, respectively. Table 8 uses the reset-horizon protocol

after delay alignment and valid-origin screening, whereas Table 9 uses mode-conditioned one-step validation. Results obtained under different protocols are not compared directly.

Table 5. PhysGuard model-selection result. Scores are calculated from unrounded RMSE values using (29); a lower score indicates better held-out rollout performance.

Model	μ	RMSE_{80} (mm)	RMSE_{120} (mm)	S_V^{sel}	Decision
Warm start	0.000	0.38219	0.59611	0.0420309	Selected
Bounded-refinement candidate	1.000	0.43144	0.66188	0.0471345	Rejected

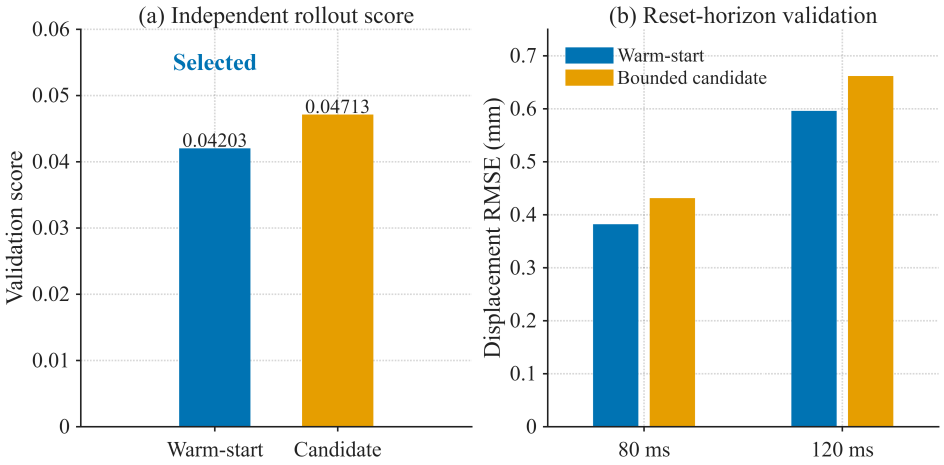


Figure 11. PhysGuard predictor selection. The bounded-refinement candidate is rejected because its held-out validation score is higher than that of the warm-start predictor.

Table 6. Validation components under the dense multi-origin sensitivity protocol.

Predictor	RMSE_{80} (mm)	RMSE_{120} (mm)	$E_{\max}$ (mm)	N_{80}	N_{120}
Warm-start	0.3282	0.5294	6.0031	19,970	29,925
Bounded-refinement candidate	0.3652	0.5801	6.6405	19,970	29,925

Relative to the warm start, the bounded-refinement candidate increases RMSE_{80}, RMSE_{120}, and $E_{\max}$ by 11.27%, 9.58%, and 10.62%, respectively. In Table 7, each component is normalized as $\rho_j(\theta) = m_j(\theta)/m_j(\theta_0)$, $j \in \{80, 120, \max\}$, and S_V^{ratio} is their weighted sum. The maximum-error term penalizes isolated large rollout deviations.

Table 7. PhysGuard score-weight and guard-margin sensitivity under the dense multi-origin protocol.

Weight Case	w_{80}	w_{120}	$w_{\max}$	ϵ_g	$S_{\mathrm{warm}}^{\mathrm{ratio}}$	$S_{\mathrm{cand}}^{\mathrm{ratio}}$	Selected
Equal	0.33	0.33	0.33	0–0.010	1.0000	1.1049	Warm-start
80 ms	0.50	0.25	0.25	0–0.010	1.0000	1.1068	Warm-start
120 ms	0.25	0.50	0.25	0–0.010	1.0000	1.1026	Warm-start
Max error	0.25	0.25	0.50	0–0.010	1.0000	1.1052	Warm-start
RMSE	0.45	0.45	0.10	0–0.010	1.0000	1.1044	Warm-start

Table 7 and Figure 12 show that all tested score-weight and guard-margin settings select the warm-start predictor.

The final selected predictor is evaluated under the reset-horizon validation protocol after delay alignment, valid-origin screening, and mode assignment. Table 8 reports RMSE, mean absolute error (MAE), maximum absolute error, and modal counts. The higher error at 120 ms indicates that residual model mismatch accumulates beyond the 80 ms controller horizon.

Table 8. Errors of the selected predictor under the reset-horizon validation protocol.

Reset Horizon	RMSE (mm)	MAE (mm)	Max. Error (mm)	Fit (%)	n_{pos}	n_{dead}	n_{neg}
80 ms	0.38219	0.16599	3.7001	94.318	7145	10,679	7156
120 ms	0.59611	0.22903	5.9391	91.140	7145	10,687	7158

Note: MAE denotes mean absolute error; Max. error denotes maximum absolute error.

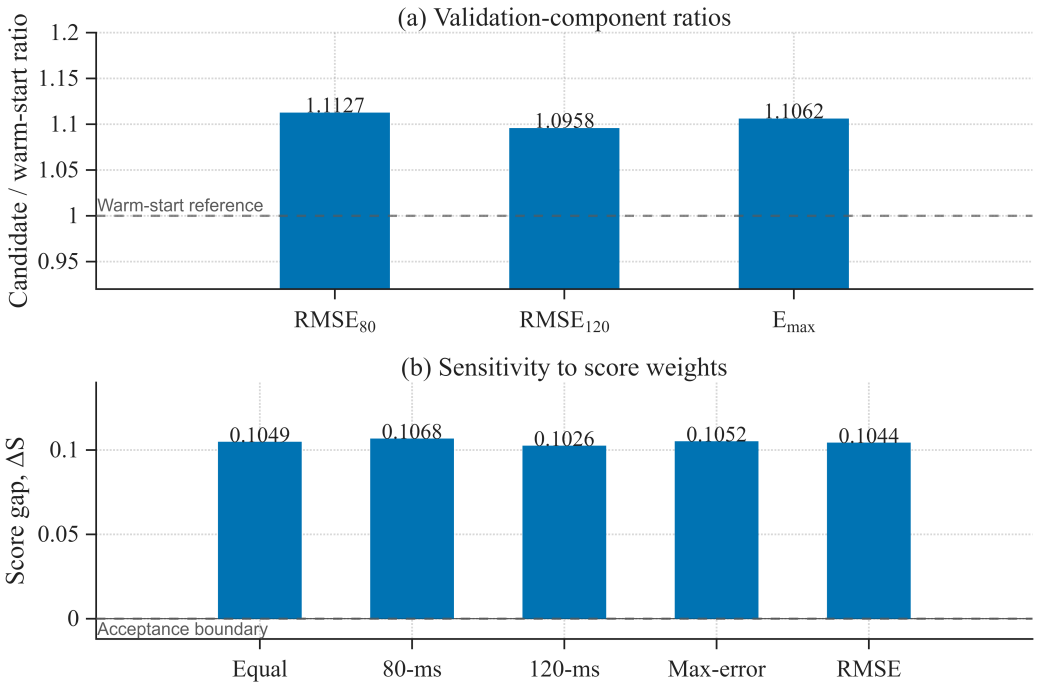


Figure 12. PhysGuard sensitivity using recorded sine-wave validation data. The normalized validation-component ratios of the bounded-refinement candidate exceed the warm-start reference. The positive ratio-score gap ($\Delta S^{\text{ratio}} = S^{\text{ratio}}_{\text{cand}} - S^{\text{ratio}}_{\text{warm}}$) remains above the acceptance boundary for all tested weight settings.

The mode-conditioned one-step protocol assigns each prediction origin from measured pilot-spool displacement using $x_{p,\text{dz}} = 0.52$ mm. The corresponding PWA branch predicts $\Delta x_{m,k+1}$, and Table 9 reports the error $(\hat{x}_{m,k+1} - x_{m,k+1})$.

Table 9. Mode-conditioned one-step prediction errors of the selected pilot-opening-scheduled PWA predictor. Modes are assigned using measured pilot-spool displacement at the prediction origin with $x_{p,\text{dz}} = 0.52$ mm.

Mode	Condition	N	RMSE (mm)	MAE (mm)	Max. Error (mm)
M1—positive opening	$x_p > 0.52$ mm	7191	0.17121	0.15177	0.23485
M2—overlap dead zone	$\lvert x_p \rvert \le 0.52$ mm	10,618	0.00930	0.00344	0.06074
M3—negative opening	$x_p < -0.52$ mm	7190	0.16893	0.14848	0.23263

Table 9 shows that the overlap/dead-zone branch has the smallest one-step error because the local motion is dominated by increment decay and centering. The positive- and negative-opening branches have larger errors, consistent with the wider active-opening residuals in Figure 8; these branches include pressure-build-up delay, asymmetric flow paths, local saturation, and direction-dependent friction. The two active branches have comparable sample support in this validation record.

5. K-DCS-ET-MPC Formulation and Control-Domain Predictor Refinement

The event-triggered finite-set controller uses the selected PWA model as its internal predictor. The complete controller is denoted as K-DCS-ET-MPC; K-DCS is the kinematic dead-zone-crossing scheduling strategy introduced in (48). The nominal Simulink plant has the same three-region PWA structure and the same 0.52 mm overlap boundary. Thus, the nominal simulation evaluates closed-loop behavior with a calibrated plant model of the same structure and is not an independent multiphysics validation.

5.1. Control-Domain Refinement and Guarded Acceptance

Before ET-MPC deployment, a bounded control-domain refinement was performed to generate a candidate model without changing the pilot-opening mode partition. The guarded selection rule then compared this candidate with the warm-start predictor on the held-out validation record described in Section 4.3.

The refinement solves

$$J = J_{\text{data}} + \lambda_{\text{reg}} J_{\text{reg}} + \lambda_{\text{edge}} J_{\text{edge}}, \tag{31}$$

where J_{data} combines tracking and transition errors, J_{reg} penalizes deviations from the nominal parameters, and J_{edge} penalizes predicted endpoint-limit violations. Section 4.3 describes the guarded evaluation of the resulting candidate. Because the candidate performed worse on the held-out selection record, it was rejected and did not alter the final online controller.

The 80 ms validation horizon matches the controller prediction horizon. The greater drift observed at 120 ms motivates a forced-refresh interval shorter than either validation horizon. Plan smoothing limits changes in the pilot reference, and stroke margins protect against endpoint impacts.

The compact controller prediction state is defined as

$$X_k = [x_{m,k}, \Delta x_{m,k}, x_{p,k}]^T, \tag{32}$$

where x_m and x_p are expressed in millimeters and $\Delta x_{m,k}$ is the predicted main-spool displacement increment per sample. The PWA rollout propagates this increment directly instead of using a continuously scaled velocity state. For a pilot-reference candidate, $O_c(x_p; x^c_{p,\text{dz}})$ denotes the controller-side overlap-compensation map. The controller and identified predictor use the same threshold of $x^c_{p,\text{dz}} = 0.52$ mm. The rollout is defined by

$$x_{p,\text{eff},k} = O_c(x_{p,k}; x^c_{p,\text{dz}}), \tag{33}$$

$$x_{n,k} = \frac{x_{m,k}}{10.620}, \tag{34}$$

$$\Delta x_{m,k+1} = g_i(\Delta x_{m,k}, x_{p,\text{eff},k}, x_{n,k}), \tag{35}$$

$$x_{m,k+1} = x_{m,k} + \Delta x_{m,k+1}, \tag{36}$$

where $g_i(\cdot)$ is the corresponding PWA increment branch scheduled by pilot opening and inherited from (17) and (18). The normalized main-spool coordinate is recomputed at each rollout step, while pressure states are not propagated online.

The direction-dependent pilot model in (7) and (8) supports cascade identification and prediction. The following servo calibration serves a different purpose: it maps the selected pilot reference to PWM within the inner loop. Thus, the two models are not alternative descriptions of the same function. The finite-set decision variable is the

pilot-spool reference ($x_{p,\mathrm{ref}}$) rather than the PWM command. After ET-MPC selects this reference, the inner pilot-spool servo generates the PWM command using

$$x_{p,k+1} = a_{\mathrm{sv}} x_{p,k} + b_{\mathrm{sv}} u_k + c_{\mathrm{sv}}, \tag{37}$$

where $a_{\mathrm{sv}} = 0.802061336$, $b_{\mathrm{sv}} = 2.749651181 \times 10^{-3}$, and $c_{\mathrm{sv}} = 3.669981716 \times 10^{-5}$. In this servo calibration, x_p is expressed in millimeters, and u_k is expressed in PWM percentage points; therefore, b_{sv} has units of millimeters per PWM percentage point.

The ET-MPC layer is solver-free and selects its decision variable from a finite set of pilot references. Measurement acquisition, filtering, error calculation, event evaluation, plan retention, smoothing, and PWM protection are executed every 4 ms. A refresh in the quiet region invokes neutral parking without a candidate search; any other refresh invokes a complete finite-set search and replaces the retained plan. If no refresh is requested, the controller reuses that plan. Figure 13 summarizes this hierarchy. Its output labeled "trigger" records complete-search requests and is the signal used for workload accounting.

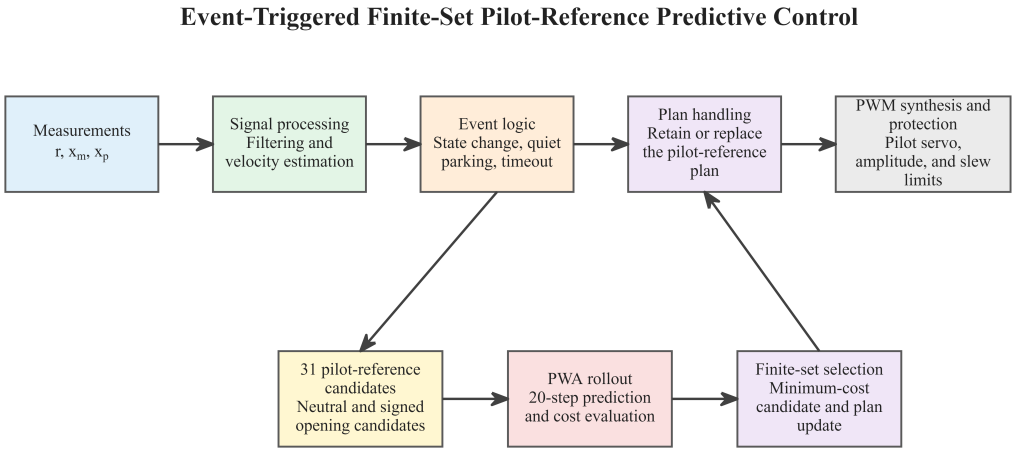


Figure 13. ET-MPC signal flow. The trigger output records complete-search requests; a refresh may instead invoke neutral parking.

At each complete-search sample, the controller evaluates a finite set of pilot-reference candidates. With the overlap threshold defined above, this set is

$$C_p = \{0\} \cup \left\{ x^c_{p,\mathrm{dz}} + \delta_j \right\}_{j=1}^{15} \cup \left\{ -x^c_{p,\mathrm{dz}} - \delta_j \right\}_{j=1}^{15}, \tag{38}$$

where

$$\begin{aligned} \{\delta_j\}_{j=1}^{15} = \{&0.001, 0.002, 0.003, 0.004, 0.005, 0.006, 0.008, 0.010, \\ &0.015, 0.030, 0.080, 0.200, 0.500, 1.200, 1.480\} \text{ mm}. \end{aligned} \tag{39}$$

With $x^c_{p,\mathrm{dz}} = 0.52$ mm, the largest-magnitude pilot-reference candidates are $\pm(0.52 + 1.480) = \pm 2.00$ mm, matching the controller's pilot-reference limit of ±2.0 mm. The controller then evaluates the PWA rollout cost over this explicit set:

$$x^{\mathrm{sel}}_{p,\mathrm{cmd},k} = \arg\min_{x^c_p \in C_p} J_k(x^c_p). \tag{40}$$

For each candidate, the rollout is initialized from the measured states and the retained displacement increment, i.e.,

$$\hat{x}_{m,k|k} = x_{m,k}, \qquad \Delta\hat{x}_{m,k|k} = \Delta x_{m,k}, \qquad \hat{x}_{p,k|k} = x_{p,k}. \tag{41}$$

During the rollout, the predicted pilot state is initialized from the measured displacement, then evolves toward the candidate reference according to

$$\hat{x}_{p,k+\ell+1} = \hat{x}_{p,k+\ell} + \beta_p \left(x_p^c - \hat{x}_{p,k+\ell} \right), \qquad \beta_p = 0.55, \tag{42}$$

The recursions in (33)–(36) are then propagated over a 20-step horizon. At each rollout step, the prediction reference is obtained by locally extrapolating the filtered reference and applying stroke-margin saturation:

$$\hat{r}_{k+\ell} = \mathrm{sat}_{[x_{\min}+0.350,\, x_{\max}-0.300]} \left(r_{f,k} + \ell T_s \dot{r}_{f,k} \right), \tag{43}$$

where $r_{f,k}$ and $\dot{r}_{f,k}$ are the filtered reference and filtered reference velocity used by the controller implementation, $x_{\min} = -10.5610$ mm, and $x_{\max} = 7.0686$ mm. At $T_s = 4$ ms, the 20-step prediction horizon is 80 ms. The maximum ordinary refresh interval is 32 ms, which is shorter than both validation horizons. Stroke margins and pilot-reference smoothing reduce endpoint impacts and overlap-region chatter. The finite-set cost is defined as

$$\begin{aligned} J_k(x_p^c) = & \sum_{\ell=1}^{19} \left[Q_x e_{k+\ell}^2 + Q_{\Delta x} \left(\Delta \hat{x}_{m,k+\ell} - \Delta x_{\mathrm{ref},k} \right)^2 \right] \\ & + Q_{x,\mathrm{term}}\, e_{k+20}^2 + Q_{\Delta x} \left(\Delta \hat{x}_{m,k+20} - \Delta x_{\mathrm{ref},k} \right)^2 \\ & + R_{\Delta x_p} \left(x_p^c - x_{p,\mathrm{plan},k-1} \right)^2 + R_{x_p} (x_p^c)^2 + J_{\mathrm{cross}} + J_{\mathrm{lim}}. \end{aligned} \tag{44}$$

Here, $e_{k+\ell} = \hat{r}_{k+\ell} - \hat{x}_{m,k+\ell}$; $\Delta x_{\mathrm{ref},k} = \mathrm{sat}_{[-0.08,0.08]}(T_s \dot{r}_{f,k})$; and the fixed weights are $Q_x = 1.00$, $Q_{\Delta x} = 0.020$, and $R_{x_p} = 0.001$. The stroke-limit penalty is

$$J_{\mathrm{lim}} = R_{\mathrm{lim}} \sum_{\ell=1}^{20} \left[\left(\hat{x}_{m,k+\ell} - x_{\max} \right)_+^2 + \left(x_{\min} - \hat{x}_{m,k+\ell} \right)_+^2 \right], \qquad R_{\mathrm{lim}} = 150.0, \tag{45}$$

where $(z)_+ = \max(z, 0)$. The penalty is zero within the permitted range and increases when a predicted trajectory violates a stroke limit. The protective weight of $R_{\mathrm{lim}} = 150$ favors feasible candidates over candidates that violate a limit and is not a tracking-tuning weight. Let $\mathbb{I}[\cdot]$ denote the indicator function, which equals one when its logical argument is true and zero otherwise. The penalty for direct reversal of the pilot-reference sign is

$$\begin{aligned} J_{\mathrm{cross}} = w_{\mathrm{cross}}\, & \mathbb{I} \left[\left(x_{p,\mathrm{plan},k-1} > x_\epsilon \ \wedge\ x_p^c < -x_\epsilon \right) \vee \left(x_{p,\mathrm{plan},k-1} < -x_\epsilon \ \wedge\ x_p^c > x_\epsilon \right) \right] \\ & \times \mathbb{I} \left[|\dot{r}_{f,k}| \le v_{\mathrm{cross}} \right], \end{aligned} \tag{46}$$

with $w_{\mathrm{cross}} = 0.800$, $x_\epsilon = 0.100$ mm, and $v_{\mathrm{cross}} = 1.20$ mm/s in the controller implementation. Thus, direct pilot-reference polarity reversal is discouraged near steady motion but is allowed during sufficiently fast commanded crossings. Kinematic dead-zone-crossing scheduling (K-DCS) identifies rapid dead-zone traversal using the following indicator:

$$\chi_{\mathrm{dz}} = \mathbb{I} \left[|x_{m,k}| < x_{\mathrm{cross}} \ \wedge\ |\dot{r}_{f,k}| > v_{\mathrm{dz}} \right], \qquad x_{\mathrm{cross}} = 2.500 \text{ mm}, \quad v_{\mathrm{dz}} = 1.50 \text{ mm/s}. \tag{47}$$

The scheduled terminal and pilot-reference move weights are

$$\left(R_{\Delta x_p}, Q_{x,\mathrm{term}} \right) = \begin{cases} (0.000,\ 30.00), & \chi_{\mathrm{dz}} = 1, \\ (0.050,\ 8.00), & \chi_{\mathrm{dz}} = 0,\ |\dot{r}_{f,k}| > 1.00 \text{ mm/s}, \\ (0.500,\ 4.50), & \chi_{\mathrm{dz}} = 0,\ |\dot{r}_{f,k}| \le 1.00 \text{ mm/s}. \end{cases} \tag{48}$$

The crossing case uses the most aggressive setting, allowing the finite search to select a large pilot-opening candidate during dead-zone traversal, while the low-speed hold case suppresses candidate chatter near steady-state extrema. Together with event-triggered plan retention, this K-DCS schedule forms the complete K-DCS-ET-MPC controller.

The event logic enforces both minimum and maximum refresh intervals. Let n_k be the number of samples elapsed since the previous refresh, and define

$$\zeta_k = \left(|r_{f,k} - r_{f,k_t}| > 0.050 \text{ mm}\right) \vee \left(|x_{m,k} - x_{m,k_t}| > 0.050 \text{ mm}\right) \vee \left(|e_{f,k} - e_{f,k_t}| > 0.060 \text{ mm}\right), \tag{49}$$

where $r_{f,k}$ is the filtered reference, $e_{f,k} = r_{f,k} - x_{m,k}$, and k_t denotes the most recent refresh sample. The zero-region parking condition is

$$\chi_{\text{quiet},k} = \mathbf{1}\left[|r_{f,k}| < 0.045 \text{ mm} \wedge |x_{m,k}| < 0.045 \text{ mm} \wedge |e_{f,k}| < 0.080 \text{ mm} \wedge |\hat{v}_{m,k}| < 0.15 \text{ mm/s}\right]. \tag{50}$$

With $N_{\min} = 2$ and $N_{\max} = 8$, the event decision is

$$\gamma_k = \mathbf{1}\left[(n_k \geq N_{\max}) \vee (n_k \geq N_{\min} \ \wedge \ \zeta_k) \vee \chi_{\text{quiet},k}\right], \tag{51}$$

Here, γ_k is the general refresh indicator, and $\chi_{\text{quiet},k}$ identifies the zero-region parking condition that restores the neutral pilot reference. For refreshes caused by state changes, the minimum and maximum intervals are 8 and 32 ms, respectively. The parking condition is combined with the other conditions through a logical OR and may therefore trigger a refresh before $N_{\min}$. When $\gamma_k = 1$, a quiet-region sample invokes only neutral parking; any other refresh invokes the 31-candidate search. When $\gamma_k = 0$, the controller skips the search and reuses the retained plan. The zero-region parking condition refreshes the neutral pilot reference when the filtered reference, measured spool displacement, tracking error, and filtered velocity are all near zero. It prevents a residual pilot-reference plan from persisting in the overlap region and is separate from the ordinary state-change trigger.

The selected pilot-reference command is first rate-limited at the planning level:

$$\begin{aligned} &x_{p,\text{plan},k} = x_{p,\text{plan},k-1} \ + \ \text{sat}_{[-\Delta x_{p,\text{plan}}, \Delta x_{p,\text{plan}}]}\left(x^{\text{sel}}_{p,\text{cmd},k} - x_{p,\text{plan},k-1}\right), \\ &\Delta x_{p,\text{plan}} = 0.250 \text{ mm}. \end{aligned} \tag{52}$$

It is then smoothed at the sample level:

$$\Delta x_{p,s,k} = \begin{cases} 1.800 \text{ mm/sample}, & \text{sign reversal or near-overlap crossing}, \\ 0.016 \text{ mm/sample}, & \text{otherwise}, \end{cases} \tag{53}$$

$$x_{p,\text{ref},k} = x_{p,\text{ref},k-1} \ + \ \text{sat}_{[-\Delta x_{p,s,k}, \Delta x_{p,s,k}]}\left(x_{p,\text{plan},k} - x_{p,\text{ref},k-1}\right), \tag{54}$$

where the larger allowance is enabled when the plan crosses sign or the smoothed pilot reference is close to the overlap boundary. In the implementation diagnostics, `dpRef` denotes the smoothed pilot reference ($x_{p,\text{ref},k}$), not a pressure-difference reference.

The final PWM synthesis is performed by the inner pilot-spool servo:

$$u_k^{\text{raw}} = \begin{cases} 0, & |x_{p,\text{ref},k}| < 0.030 \text{ mm}, \\ \dfrac{(1 - a_{\text{sv}})x_{p,\text{ref},k} - c_{\text{sv}}}{b_{\text{sv}}} + K_{xp}\left(x_{p,\text{ref},k} - x_{p,k}\right), & \text{otherwise}, \end{cases} \tag{55}$$

where $K_{xp} = 28$ PWM percentage points per millimeter for the positive/neutral branch and $K_{xp} = 22$ PWM percentage points per millimeter for the negative branch. The first term provides steady-state feedforward for the pilot reference, and the second applies

proportional feedback from the measured pilot displacement. The raw PWM command is then subjected to an amplitude limit, a plan-projection limit, and an output slew-rate limit:

$$\tilde{u}_k^{\mathrm{raw}} = \mathrm{sat}_{[-u_{\max,k},u_{\max,k}]}\left(u_k^{\mathrm{raw}}\right), \tag{56}$$

$$u_k^{\mathrm{proj}} = \mathrm{sat}_{[-u_{\max,k},u_{\max,k}]}\left[u_{k-1} + \mathrm{sat}_{[-\Delta u_{\mathrm{plan,max}},\Delta u_{\mathrm{plan,max}}]}\left(\tilde{u}_k^{\mathrm{raw}} - u_{k-1}\right)\right]. \tag{57}$$

$$u_k = \mathrm{sat}_{[-u_{\max,k},u_{\max,k}]}\left[u_{k-1} + \mathrm{sat}_{[-\Delta u_{\max,k},\Delta u_{\max,k}]}\left(u_k^{\mathrm{proj}} - u_{k-1}\right)\right]. \tag{58}$$

The $u_{\max,k}$ and $\Delta u_{\max,k}$ bounds depend on the sign of the smoothed pilot reference. The positive/neutral branch uses $u_{\max} = 62\%$ and $\Delta u_{\max} = 8.0$ PWM percentage points per sample, whereas the negative branch uses $u_{\max} = 54\%$ and $\Delta u_{\max} = 6.5$ percentage points per sample. The intermediate plan-projection limit is $\Delta u_{\mathrm{plan,max}} = 10.0$ percentage points per sample. Together, these elements form an event-triggered pilot-reference controller with finite-set rollout and inner-loop PWM synthesis. For workload accounting, the complete-search flag records execution of the 31-candidate search. The general refresh indicator additionally records neutral-parking updates that bypass the candidate loop. The fixed implementation parameters are summarized in Table 10. The amplitude and slew-rate limits in (58) are actuator-protection bounds, not PhysGuard decision variables. Sensor and communication specifications are reported separately in Section 5.7.

Table 10. Fixed implementation parameters of the proposed K-DCS-ET-MPC.

Parameter Group	Fixed Settings
Sampling and event logic	$T_s = 4$ ms; $N_{\min} = 2$; $N_{\max} = 8$; ordinary refresh interval 8–32 ms; thresholds 0.050 mm for r_f and x_m and 0.060 mm for e_f; zero-region parking defined by (50).
Finite-set rollout	$N_p = 20$ (80 ms); $x^c_{p,\mathrm{dz}} = 0.52$ mm; 31 candidates from (38) and (39); $\beta_p = 0.55$; $\Delta x_{\mathrm{ref}} \in [-0.08, 0.08]$ mm/sample; reference stroke margins $x_{\min} + 0.350$ mm and $x_{\max} - 0.300$ mm.
K-DCS and protection	$R_{\mathrm{lim}} = 150$; $w_{\mathrm{cross}} = 0.800$; $x_\epsilon = 0.100$ mm; $v_{\mathrm{cross}} = 1.20$ mm/s; $x_{\mathrm{cross}} = 2.500$ mm; $v_{\mathrm{dz}} = 1.50$ mm/s; $\Delta x_{p,\mathrm{plan}} = 0.250$ mm/sample; $\Delta x_{p,s} = 0.016$ mm/sample; reversal allowance 1.800 mm.
Pilot servo	$K_{xp} = 28$ for the positive/neutral branch and 22 for the negative branch; zero sample delay in both the pilot- and main-spool channels; neutral band $\lvert x_{p,\mathrm{ref}}\rvert < 0.030$ mm.

A separate 10 s sensitivity sweep varied R_{lim}, the prediction horizon, pilot-reference smoothing, and PWM rate limits individually. Two combined cases varied these parameters, together with the stroke margins. Table 11 reports metrics calculated offline over $t \in [5, 10]$ s; comparisons are restricted to cases within this sweep.

Within the tested range, R_{lim} does not affect the reported metrics at the displayed precision because the predicted trajectory does not enter the stroke-penalty region. The prediction horizon produces the largest variation: $N_p = 15$ reduces the reported errors, whereas $N_p = 25$ increases them. The nominal value of $N_p = 20$ is retained because it was fixed before the common evaluation and matches the 80 ms validation horizon; the sweep was not used for retuning.

5.2. Complete-Search Reduction Accounting

The computational effect of the event-triggered layer is quantified by its complete-search count relative to TT-MPC, which performs a complete finite-set search at every sampling instant. Because the simulation stores samples from $t = 0$ to $t = T_{\mathrm{sim}}$ inclusively, the TT-MPC search count for a simulation length of T_{sim} and sampling period T_s is

$$N_{\text{total}} = \frac{T_{\text{sim}}}{T_s} + 1. \tag{59}$$

The K-DCS-ET-MPC implementation executes the complete pilot-reference search only when the complete-search flag is active. Let N_{search} denote the number of samples at which the 31-candidate search is executed. Neutral parking refreshes bypass the candidate loop and are counted separately. The complete-search reduction ratio is

$$\eta = \left(1 - \frac{N_{\text{search}}}{N_{\text{total}}}\right) \times 100\%. \tag{60}$$

Each complete search evaluates the same 31 candidates, so η also gives the reduction in candidate rollouts. However, η should not be interpreted as a reduction in processor time because acquisition, filtering, event evaluation, plan propagation, smoothing, saturation, and PWM synthesis still run at every sample. Target-processor time and utilization were not recorded during the bench test. Over the full 20 s record, TT-MPC executes 5001 complete searches, whereas K-DCS-ET-MPC issues 1029 refreshes and executes 1025 complete searches. The corresponding reductions relative to TT-MPC are 79.4% in refreshes and 79.5% in complete searches. The mean and maximum refresh intervals are 19.44 and 32.0 ms, respectively (Table 12).

Table 11. Protection-parameter sensitivity of the proposed controller in a separate 10 s sweep. Metrics are evaluated over $t \in [5, 10]$ s.

Case	MAE (mm)	RMSE (mm)	Max. Error (mm)	Reduction (%)
Nominal	0.0221	0.0297	0.1268	78.97
$R_{\text{lim}} = 100$	0.0221	0.0297	0.1268	78.97
$R_{\text{lim}} = 200$	0.0221	0.0297	0.1268	78.97
$N_p = 15$	0.0137	0.0212	0.1180	79.25
$N_p = 25$	0.0397	0.0631	0.2701	78.85
Slow smoothing	0.0215	0.0309	0.1464	79.09
Fast smoothing	0.0214	0.0311	0.1431	79.13
Tight PWM rate	0.0222	0.0310	0.1299	79.01
Loose PWM rate	0.0212	0.0307	0.1340	78.97
Conservative combined	0.0309	0.0441	0.2247	78.81
Aggressive combined	0.0141	0.0217	0.1208	79.17

Note: Conservative combined: $R_{\text{lim}} = 200$; $N_p = 25$; safe stroke margins, $(0.500, 0.500)$ mm; reference stroke margins, $(0.400, 0.450)$ mm; $(\Delta x_{p,\text{plan}}, \Delta x_{p,s}, \Delta x_{p,\text{rev}}) = (0.200, 0.012, 1.200)$ mm/sample; $(\Delta u_{\text{plan}}, \Delta u_{+}, \Delta u_{-}) = (8.0, 6.0, 5.0)$ percentage points/sample. Aggressive combined: $R_{\text{lim}} = 100$; $N_p = 15$; safe stroke margins, $(0.300, 0.300)$ mm; reference stroke margins, $(0.220, 0.270)$ mm; smoothing, $(0.300, 0.020, 2.000)$ mm/sample; PWM-rate limits, $(12.0, 10.0, 8.0)$ percentage points/sample. Smoothing, PWM-rate, and combined cases are sensitivity probes; the sweep was not used to retune the reported controller.

Table 12. Refresh and complete finite-set search counts over the 20 s closed-loop simulation.

Strategy	Refresh Requests	Complete Searches	Mean Refresh Interval (ms)	Reduction (η)
TT-MPC (time-triggered)	5001	5001	4.00	Baseline
Proposed K-DCS-ET-MPC	1029	1025	19.44	79.5%

The inter-refresh interval distribution and complete-search counts are shown in Figures 14 and 15, respectively.

Offline timing used MATLAB R2025b on a Windows 11 host with an AMD Ryzen 7 H255 processor. From the 1025 complete searches in the 20 s simulation, 500 uniformly sampled states were each evaluated 20 times after 300 warm-up calls,

giving 10,000 timed executions. The measured `tic–toc` overhead of 0.2 µs was subtracted. The timing covers the 31-candidate search and immediate plan limiting but excludes Simulink solution, plotting, file I/O, trigger evaluation, smoothing, and PWM synthesis. It is therefore a host-side reference for the search routine, not a target-MCU execution-time measurement.

Table 13 shows that the mean and 99th-percentile search times are 2.46% and 4.79% of the 4 ms period, respectively, and that the maximum remains below one period. These values apply only to the host replay.

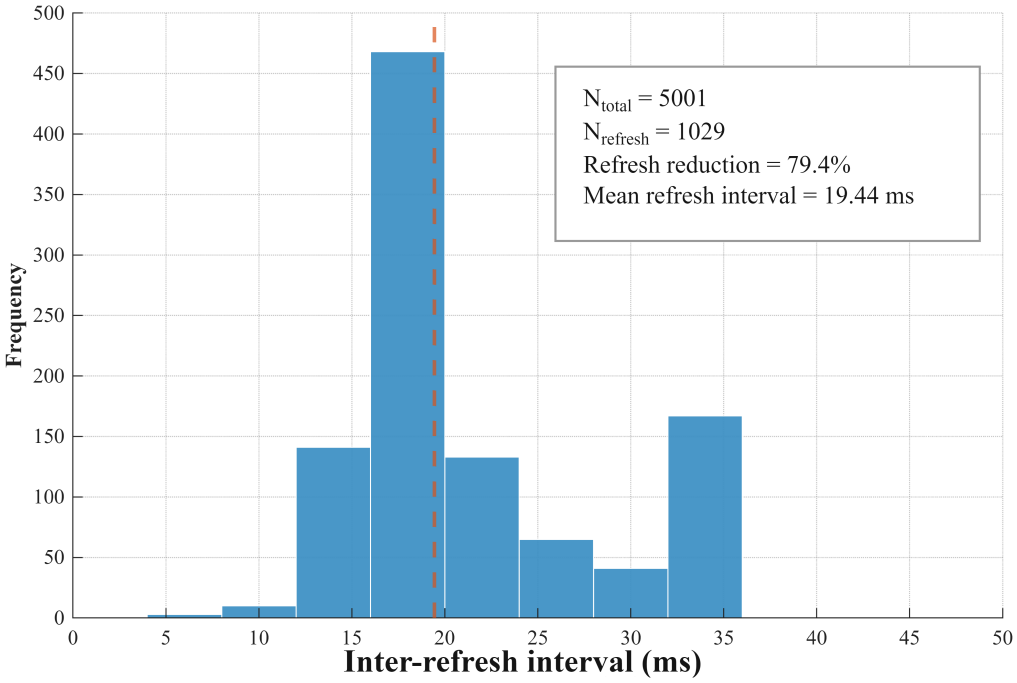


Figure 14. Inter-refresh interval distribution under the forced-refresh constraint. The orange dashed vertical line marks the mean refresh interval of 19.44 ms.

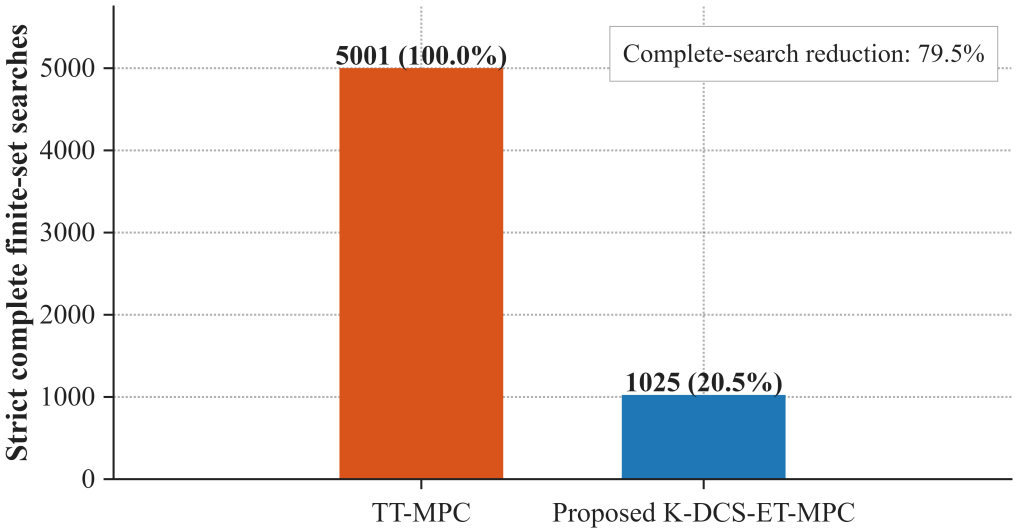


Figure 15. Complete finite-set search counts for TT-MPC and the proposed K-DCS-ET-MPC.

5.3. Post-Transient Two-Period Window Analysis

The full 20 s record includes startup and large transients. Post-transient cyclic behavior is therefore evaluated separately in a two-period window selected by the deterministic

RMSE criterion below. Let $\mathcal{K}_{\mathrm{ss}}$ denote the set of feasible post-transient starting indices satisfying $k_0 + N_w - 1 \le N_{\mathrm{sim}}$. The selected window is

$$k_{\mathrm{win}} = \arg\min_{k_0 \in \mathcal{K}_{\mathrm{ss}}} \sqrt{\frac{1}{N_w} \sum_{\ell=0}^{N_w-1} e_{k_0+\ell}^2}, \qquad \mathcal{W} = \{k_{\mathrm{win}}, \ldots, k_{\mathrm{win}} + N_w - 1\}. \tag{61}$$

For this window, the tracking metrics are computed as

$$\begin{aligned} \mathrm{MAE}_{\mathcal{W}} &= \frac{1}{N_w} \sum_{k \in \mathcal{W}} |e_k|, \\ \mathrm{RMSE}_{\mathcal{W}} &= \sqrt{\frac{1}{N_w} \sum_{k \in \mathcal{W}} e_k^2}, \\ e_{\max,\mathcal{W}} &= \max_{k \in \mathcal{W}} |e_k|. \end{aligned} \tag{62}$$

The corresponding complete finite-set search-reduction ratio in the same window is

$$\eta_{\mathcal{W}} = \left(1 - \frac{N_{\mathrm{search},\mathcal{W}}}{N_w}\right) \times 100\%. \tag{63}$$

The selected window contains $N_w = 3000$ samples, spans approximately $t \in [6.94, 18.93]$ s, and includes 450 complete searches. The resulting search reduction is $\eta_{\mathcal{W}} = 85.0\%$, with an average interval of 26.67 ms. The tracking metrics are $\mathrm{MAE}_{\mathcal{W}} = 0.0206$ mm, $\mathrm{RMSE}_{\mathcal{W}} = 0.0367$ mm, and $e_{\max,\mathcal{W}} = 0.1704$ mm. Tables 14 and 15 summarize these values, and Figure 16 shows the corresponding time histories. Because the window is selected by minimizing RMSE, its metrics are treated as auxiliary post-transient results. The primary computation count uses the full 20 s record, and the comparison of all nine controllers uses the common interval of $t \in [5, 10]$ s.

Table 13. Host-side timing of one complete finite-set search relative to the 4 ms control period.

Statistic	Complete-Search Time (µs)	Fraction of 4 ms (%)
Mean	98.6	2.46
Median	86.2	2.16
95th percentile	149.5	3.74
99th percentile	191.7	4.79
Maximum	942.8	23.57

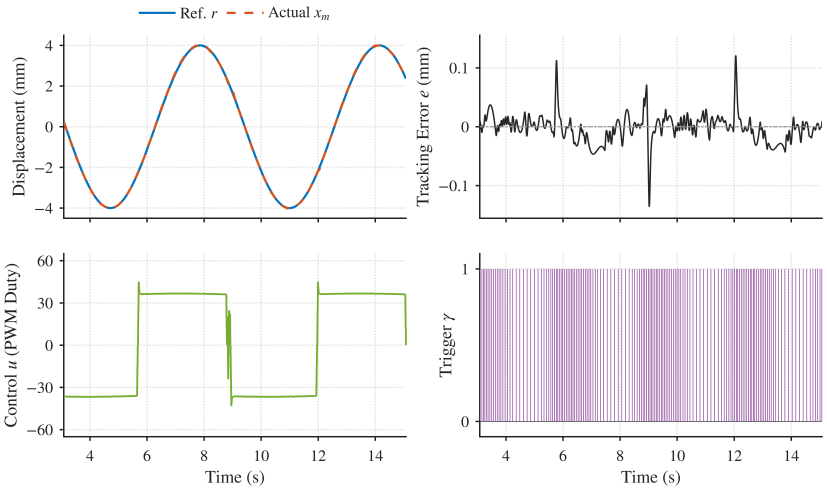


Figure 16. Reference, displacement, tracking error, PWM command, and trigger-count density in the selected post-transient two-period window. In the upper-left panel, the blue solid line is the reference

and the orange dashed line is the main-spool displacement; the black line in the upper-right panel is tracking error, the green line in the lower-left panel is PWM duty, and the purple impulses in the lower-right panel indicate trigger events.

Table 14. Complete finite-set search counts in the selected post-transient two-period simulation window.

Strategy	Complete Searches	Average Interval (ms)	Reduction (η_W)
TT-MPC (time-triggered)	3000	4.00	Baseline
Proposed K-DCS-ET-MPC	450	26.67	85.0%

Table 15. Tracking metrics in the selected post-transient two-period window.

Control Strategy	MAE (mm)	RMSE (mm)	Max. Error (mm)
Proposed K-DCS-ET-MPC	0.0206	0.0367	0.1704

5.4. Bidirectional Step-Response Simulation Analysis

A separate large-amplitude bidirectional step test evaluates dead-zone crossing, polarity reversal, and return-to-center motion. The reference alternates between the neutral position and prescribed positive and negative step levels; the evaluation window is $t \in [1.55, 15.20]$ s.

For the step-response test, the reduction in complete finite-set searches is computed as

$$\eta_{\text{step}} = \left(1 - \frac{N_{\text{search,step}}}{N_{\text{TT,step}}}\right) \times 100\%. \tag{64}$$

Here, $N_{\text{TT,step}}$ is the TT-MPC complete-search count over the same step-response evaluation window. For each step at time t_s, the normalized response coordinate is defined as $\xi(t) = (x_m(t) - r_{\text{old}})/(r_{\text{new}} - r_{\text{old}})$. The rise/fall time is evaluated from the 10–90% crossing interval. The settling time is the earliest entry into the configured tolerance band after which the response remains inside the band for a fixed dwell time:

$$\begin{aligned} t_r &= t_{0.9} - t_{0.1}, \\ t_{\text{set}} &= \inf_{\tau \geq t_s} \Big\{ \tau - t_s : \ |x_m(t) - r_{\text{new}}| \leq \max(\varepsilon_{\text{set}} |r_{\text{new}} - r_{\text{old}}|, \varepsilon_{\text{abs}}), \\ &\qquad \forall t \in [\tau, \tau + T_{\text{dwell}}] \subseteq [t_s, t_{\text{seg,end}}] \Big\}. \end{aligned} \tag{65}$$

Here, $t_{\text{seg,end}}$ denotes the end of the step segment, $\varepsilon_{\text{set}} = 0.02$, $\varepsilon_{\text{abs}} = 0.05$ mm, and $T_{\text{dwell}} = 0.08$ s, matching the MATLAB calculation. If no qualifying dwell interval exists within the segment, the transition is marked as unsettled.

Figure 17 shows that the controller tracks each large command reversal while maintaining event-triggered operation. Table 16 reports 1751 complete searches for K-DCS-ET-MPC and 3412 complete searches for TT-MPC. These values give $\eta_{\text{step}} = 48.7\%$ and an average complete-search interval of 7.80 ms. The search-count reduction is lower than that obtained during sinusoidal tracking because the step edges repeatedly activate the crossing and reversal logic.

Table 16. Complete finite-set search counts in the bidirectional step-response window.

Strategy	Complete Searches	Average Interval (ms)	Reduction η_{step}
TT-MPC (time-triggered)	3412	4.00	Baseline
Proposed K-DCS-ET-MPC	1751	7.80	48.7%

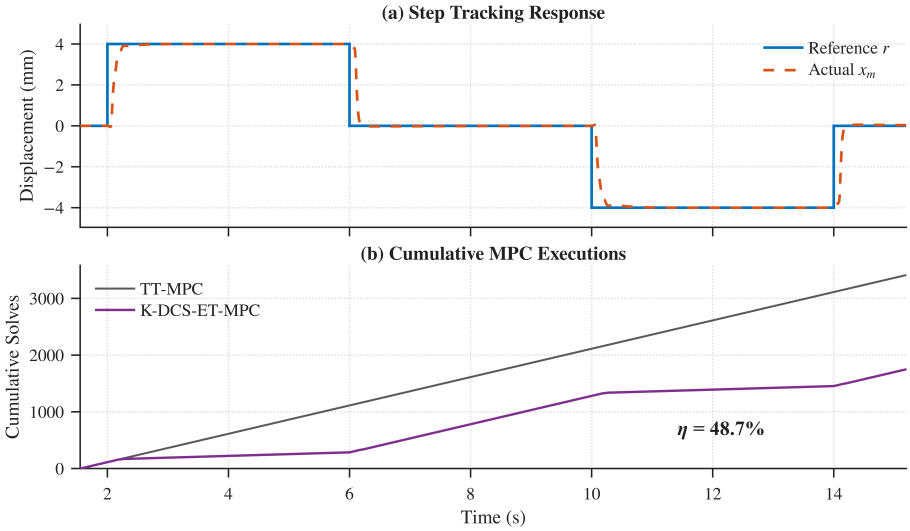


Figure 17. Bidirectional step response during dead-zone traversal, polarity reversal, and return-to-center motion.

In Table 17, overshoot (OS) denotes the overshoot percentage relative to the corresponding step amplitude. The rise and fall times range from 0.0560 to 0.1400 s, and the settling times range from 0.1920 to 0.5400 s. Because the reference is discontinuous, response-delay metrics are reported rather than integral tracking errors across the transitions.

Table 17. Rise, fall, and settling-time metrics for the bidirectional step transitions.

No.	t_s (s)	r_{old} (mm)	r_{new} (mm)	t_r (s)	t_{set} (s)	OS (%)
1	2.000	0.00	4.00	0.1400	0.4040	0.00
2	6.000	4.00	0.00	0.0600	0.1960	0.70
3	10.000	0.00	−4.00	0.1320	0.5400	0.00
4	14.000	−4.00	0.00	0.0560	0.1920	1.31

5.5. Controller Comparison and Ablation Study

Nine controllers are evaluated on the same simulated valve model and reference segment. The baselines comprise a dead-zone-compensated proportional–integral–derivative controller (DZ-PID) with $K_p = 2.8$, $K_i = 1.5$, $K_d = 0.05$, and $x^c_{p,\text{dz}} = 0.52$ mm; sliding mode control; linear FS-MPC; a piecewise lookup controller; adaptive FS-MPC; and TT-MPC with time-triggered finite-set updates.

Two matched cases provide controlled comparisons of the selected architectural features. FW-ET-MPC uses the same event-triggered structure but fixed weights; comparison with this controller assesses the influence of the reference-velocity-scheduled K-DCS weights. Full-rate K-DCS-MPC retains the candidate set, PWA rollout, K-DCS scheduling, stroke-limit penalty, pilot-reference smoothing, and PWM synthesis of the proposed controller but disables event-triggered plan reuse and executes a complete search at every non-parking sample. Comparison with this controller assesses the influence of event-triggered plan retention.

The baseline controllers use the fixed configurations listed in Table 18.

For clarity, implementation details not contained in the compact table are grouped by function:

(i) Candidate sets and adaptation: Linear FS-MPC uses $\{0\} \cup \{\pm(0.52 + \delta^{\text{lin}}_j)\}$ mm, where $\delta^{\text{lin}}_j \in \{0.002, 0.006, 0.015, 0.040, 0.080, 0.160, 0.300, 0.550, 0.900, 1.300\}$ mm. The lookup controller uses thresholds of 0.06/0.16/0.35/0.70 and offsets of 0/0.006/0.015/0.035/0.070 mm. Adaptive FS-MPC uses the 31-point set in (38) and (39); with $e_{p,k}$ =

$\mathrm{sat}_{[-2,2]}(x_{m,k} - \hat{x}_{m,k|k-1})$, its active gains are updated by $g_{\pm,k+1} = \mathrm{sat}_{[0.70,1.30]}(g_{\pm,k} \pm 0.018e_{p,k})$.

(ii) Scheduled MPC weights: For TT-MPC, $f_e = \min(|e|/0.30, 1)$. Outside zero-region parking, $Q_x = 20 + 60f_e$, $Q_{\mathrm{term}} = 20 + 180f_e$, and $R_{x_p} = 0.001$. For $|e| \le 0.30$ mm, $R_{\Delta x_p} = 0.800 - 0.790f_e$ for a static reference and $0.100 - 0.090f_e$ otherwise; for larger errors, $(Q_x, Q_{\mathrm{term}}, R_{\Delta x_p}) = (80, 200, 0.010)$. The zero-region values are $(Q_x, Q_{\mathrm{term}}, R_{\Delta x_p}, R_{x_p}) = (2, 2, 2, 0.150)$. FW-ET-MPC uses the event thresholds, refresh bounds, smoothing, and PWM protection stated in Section 5.

(iii) Shared actuation layer: Sliding mode control, linear FS-MPC, and adaptive FS-MPC use the calibrated pilot-spool servo, neutral band, stroke protection, and branch PWM limits described in Section 5. The lookup controller uses the same structure but limits PWM changes to 2.5 percentage points per sample. Its direction is selected from $d_s = e + 0.020\dot{r}_f - 0.080v_m$ with the hysteresis band $(\pm[0.060 + 0.010\min(|\dot{r}_f|, 8)])$ and is reset when $|e| < 0.035$ mm and $|\dot{r}_f| < 0.20$ mm/s.

Table 18. Fixed configurations of the additional simulation baselines.

Controller	Structure and Update Rule	Main Fixed Parameters
Sliding Mode Control	Sign-scheduled saturated pilot reference with $s = 2.20\,e + (\dot{r}_f - v_m)$	$\phi = 0.55$, $k_S = 0.80$, $k_E = 0.10$, $x_{p,\max} = 1.55$ mm, and $\Delta x_{p,s} = 0.020$ mm/sample.
Linear FS-MPC	Full-rate 21-candidate search using $\Delta x_{m,k+1} = 0.780\Delta x_{m,k} + 0.560x_{p,\mathrm{eff}} - 0.0125x_{n,k}$	$N_p = 20$, $Q_x = 10.0$, $Q_{\Delta x} = 0.020$, $Q_{\mathrm{term}} = 25.0$, $R_{\Delta x_p} = 0.120$, $R_{x_p} = 0.010$, and $R_{\mathrm{lim}} = 150$.
Piecewise lookup controller	Error- and velocity-scheduled pilot-opening lookup without an online finite-set search	$d = 0.22\|e\| + 0.025\|\dot{r}_f\| + 0.025\|\dot{r}_f - v_m\|$; four error thresholds; $\Delta x_{p,s} = 0.010$ mm/sample.
Adaptive FS-MPC	Full-rate 31-candidate PWA search with bounded branch-gain adaptation	$N_p = 20$, $Q_x = 1.20$, $Q_{\Delta x} = 0.020$, $Q_{\mathrm{term}} = 8.0$, $R_{\Delta x_p} = 0.080$, $R_{x_p} = 0.002$, $R_{\mathrm{lim}} = 150$, adaptation rate 0.018, and gain bounds 0.70–1.30.
TT-MPC	Time-triggered 31-candidate PWA search at every sampling instant; the previous pilot reference enters the move-suppression term	$N_p = 20$, $\beta_p = 0.55$, $Q_{\Delta x} = 0.020$, $R_{\mathrm{lim}} = 150$, $\Delta x_{p,\mathrm{plan}} = 10$ and $\Delta x_{p,s} = 5$ mm/sample, $\|u\| \le 62\%$, and $\|\Delta u\| \le 8$ percentage points/sample.
FW-ET-MPC	Event rule and 31-candidate PWA search of the proposed controller, with fixed cost weights	$N_p = 20$, $\beta_p = 0.55$, $Q_x = 30$, $Q_{\mathrm{term}} = 60$, $Q_{\Delta x} = 0.020$, $R_{\Delta x_p} = 0.300$, $R_{x_p} = 0.050$, and $R_{\mathrm{lim}} = 150$.

Table 19 shows that the proposed K-DCS-ET-MPC achieves the lowest MAE and RMSE over the common 5–10 s simulation window, at 0.0371 mm and 0.0569 mm, respectively. Relative to full-rate K-DCS-MPC in the same window, it reduces the number of complete searches from 1251 to 373, a reduction of 70.18%, while also reducing the RMSE from 0.0696 mm to 0.0569 mm. The proposed controller also gives lower MAE and RMSE than FW-ET-MPC under comparable event-triggered operation. Linear FS-MPC produces the smallest maximum absolute error of 0.1908 mm. Search-count reduction is reported only for controllers that perform a comparable online finite-set search; the lookup controller has a different computational structure and is therefore not assigned a reduction percentage. Figure 18 shows the full-interval and synchronized zoomed comparisons for all nine controllers.

5.6. Robustness Assessment Under Plant and Measurement Variations

The simulations perturb coefficients of the calibrated plant model as surrogates for changes in viscosity, supply/load pressure, leakage, friction/dead-zone behavior, and measurement noise. These cases assess plant–predictor mismatch within the reduced PWA structure; they do not represent direct thermofluid or hardware perturbation tests.

Table 19. Controller comparison over $t \in [5, 10]$ s under the common simulation benchmark. Complete finite-set search reduction is relative to the full-rate K-DCS-MPC baseline where a comparable online search count is defined.

Controller	MAE (mm)	RMSE (mm)	Max. Error (mm)	Complete Searches (Ratio %)	Reduction (%)
DZ-PID	0.0831	0.1050	0.3337	–	–
Sliding mode control	0.4486	0.4761	0.7421	–	–
TT-MPC	0.0713	0.0790	0.1951	1251 (100.00)	0.00
Linear FS-MPC	0.0806	0.0954	0.1908	1251 (100.00)	0.00
Piecewise lookup controller	0.4496	0.5103	1.2524	lookup	–
Adaptive FS-MPC	0.0512	0.0755	0.3027	1251 (100.00)	0.00
FW-ET-MPC	0.0583	0.0965	0.3759	384 (30.70)	69.30
Full-rate K-DCS-MPC	0.0481	0.0696	0.3004	1251 (100.00)	0.00
Proposed K-DCS-ET-MPC	0.0371	0.0569	0.2656	373 (29.82)	70.18

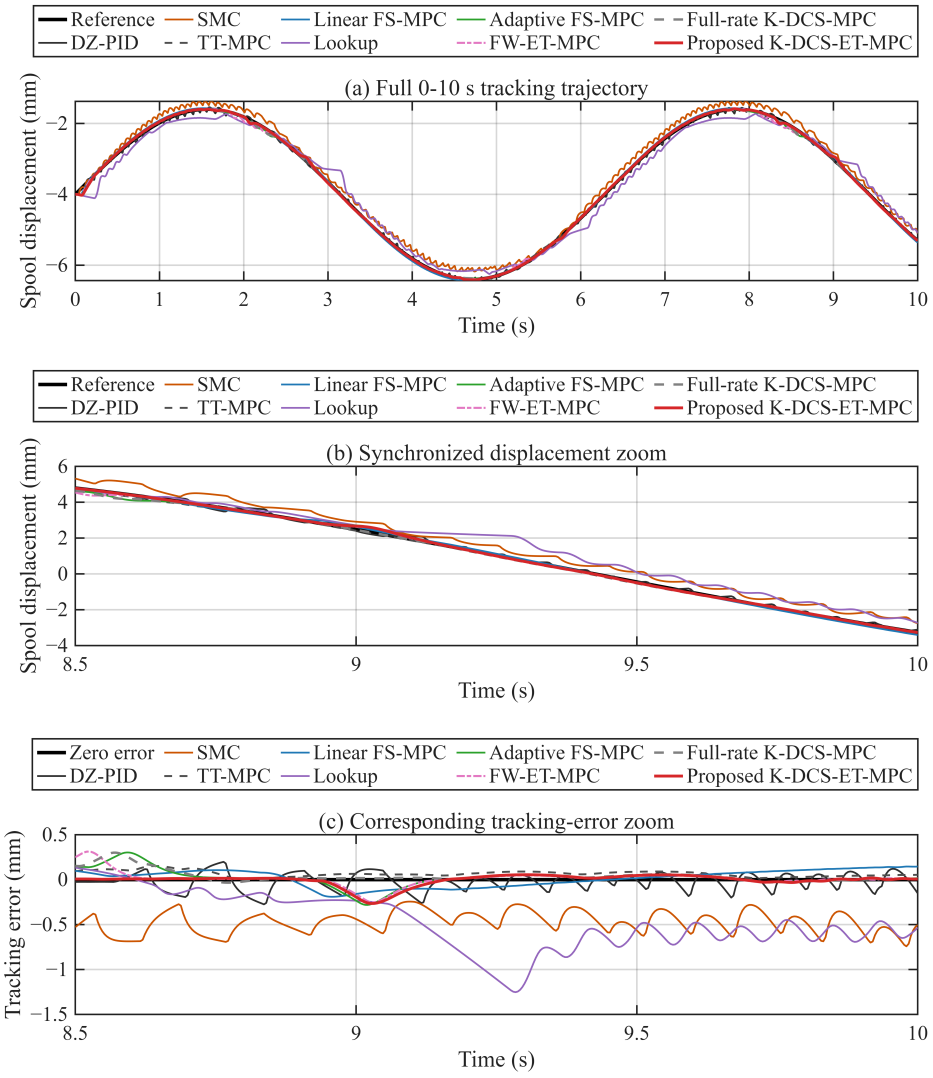


Figure 18. Controller comparison under the common simulation benchmark: (**a**) full 0–10 s tracking trajectory; (**b**) synchronized displacement zoom; (**c**) corresponding tracking-error zoom. The legend lists the reference and all nine controllers one-to-one using the same line colors and styles in every panel. The quantitative metrics in Table 19 are evaluated over $t \in [5, 10]$ s.

Robustness is assessed through simulations over $t \in [0.5, 20]$ s, with the nominal case used as the baseline. Table 20 lists the parameter changes, and Table 21 reports the resulting tracking metrics.

Table 20. Surrogate perturbation settings used in the robustness assessment.

Case	Changed Terms	Applied Perturbation
Supply/load	Active-branch drive $b_x^{(1)}$, $b_x^{(3)}$	−20%
Leakage/pressure decay	Active memory $a_\Delta^{(1)}$, $a_\Delta^{(3)}$; overlap memory $a_\Delta^{(2)}$; $\lvert k_x^{(i)}\rvert$	−15%; −30%; +10%, respectively
Viscosity	Active memory; active-branch drive; $\lvert k_x^{(i)}\rvert$	−10%; −20%; +20%, respectively
Friction/dead zone	$\lvert k_x^{(i)}\rvert$; residual offsets $c^{(i)}$; plant-side $x_{p,\mathrm{dz}}$	+15%; +30%; 0.52 → 0.55 mm
Sensor noise	Main- and pilot-spool measurements	Zero-mean noise: σ_{x_m} = 0.05 mm and σ_{x_p} = 0.02 mm
Combined	Active memory; active drive; overlap memory; $\lvert k_x^{(i)}\rvert$; $c^{(i)}$; pilot memory and input gain; $x_{p,\mathrm{dz}}$; sensor noise	−15%; −20%; −30%; +20%; +30%; +5% and −10%; 0.55 mm; noise as above

Note: Percentages are relative to the nominal calibrated simulation plant. Active branches are modes M1 and M3.

Table 21. Robustness results for the nominal and perturbed closed-loop simulations. N_{search} is the complete finite-set search count; reduction is relative to full-rate finite-set search.

Case	RMSE (mm)	MAE (mm)	$\lvert e\rvert_{\max}$ (mm)	N_{search}	Reduction (%)	Saturation (%)
Nominal	0.0282	0.0207	0.1373	984	79.8	0.0
Supply/load surrogate	0.0903	0.0816	0.1686	983	79.8	0.0
Leakage/pressure-decay surrogate	0.0940	0.0816	0.2423	986	79.8	0.0
Viscosity surrogate	0.1384	0.1288	0.2229	966	80.2	0.0
Friction/dead-zone surrogate	2.0007	1.8945	2.6138	1274	73.9	0.0
Sensor-noise variation	0.2898	0.2816	0.3974	1011	79.3	0.0
Combined multi-perturbation	0.6124	0.4856	1.0236	1012	79.2	0.0

All simulated perturbation cases remain bounded without actuator saturation. Complete-search reduction remains between 79.2% and 80.2%, except in the friction/dead-zone case, where it decreases to 73.9%. This case also produces the largest RMSE of 2.0007 mm, indicating that overlap and friction uncertainty are the dominant limitations among the tested perturbations. Persistent changes in overlap or friction may require re-identification or controller retuning. Figure 19 shows representative viscosity, sensor-noise, and combined perturbation responses.

5.7. Bench Tracking Test Under Nominal Operating Conditions

A bench tracking test was conducted on the electro-hydraulic proportional-valve platform shown in Figure 20. The platform includes the hydraulic circuit, proportional valve, controller, host computer, controller area network (CAN) acquisition card, and an external data-acquisition instrument. The proposed K-DCS-ET-MPC was executed on an S32K144-based controller under nominal operating conditions. Because synchronized logs of trigger events and execution times were not recorded, the bench test is not used to quantify complete-search reduction or target-processor timing.

The displacement sensors and their demodulation circuits are integrated with the onboard controller. The internal analog-to-digital converter (ADC) acquires the main-spool displacement, which is transmitted to the host computer through the CAN logging link at a nominal rate of 1 kHz. For offline analysis, the logged feedback channels are resampled and aligned to the 4 ms grid used by the real-time control task. During the bench test, measurement acquisition, prediction, event evaluation, and control updates were executed

at T_s = 4 ms (250 Hz). The embedded schedule also includes sensor processing, triggered rollout, PWM synthesis, and communication.

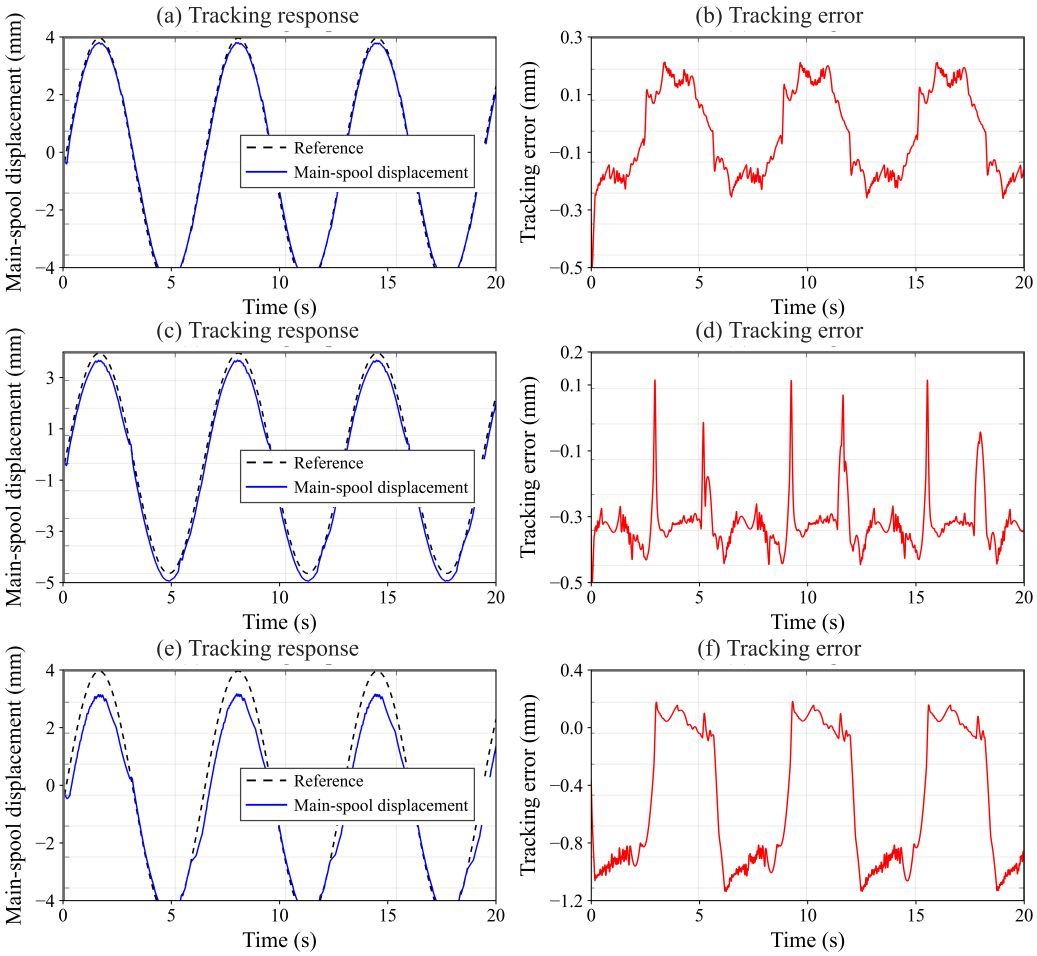
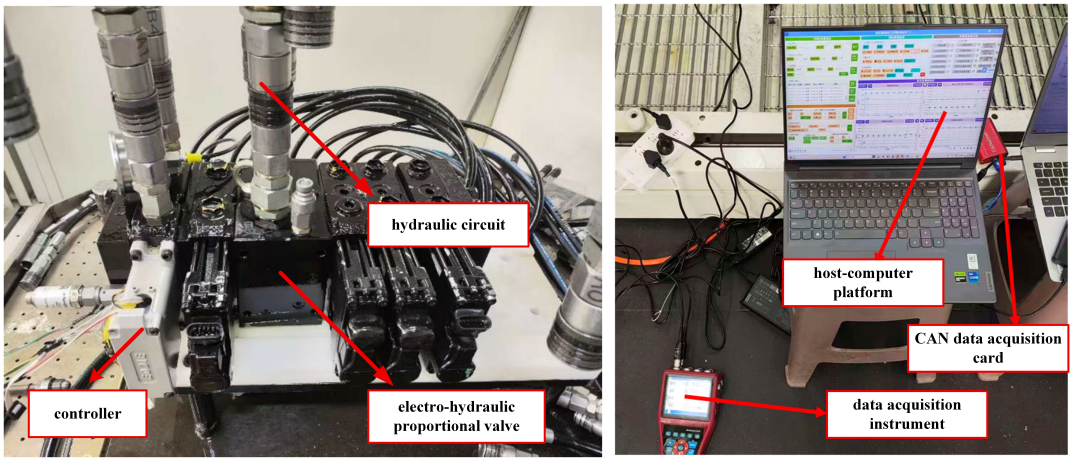


Figure 19. Representative robustness simulations: (**a**,**b**) viscosity surrogate; (**c**,**d**) sensor-noise variation; and (**e**,**f**) combined multi-perturbation. In each pair, the left panel shows the dashed black reference and blue main-spool displacement, while the right panel shows the red tracking-error line. The friction/dead-zone surrogate is reported in Table 21.

Table 22 summarizes the measurement and communication channels. Pilot- and main-spool displacements are used for mode scheduling, control feedback, and tracking evaluation, with all analyzed channels aligned to the 4 ms controller grid.

Figure 21 shows the first 100 s of measured main-spool displacement for a sinusoidal reference with an amplitude of 5.5 mm. This interval is displayed for visual clarity. The aggregate metrics use the entire retained record, whereas the cycle-level metrics use the three complete cycles after excluding the partial cycles at both ends. The largest phase lag and local tracking deviations occur where the reference slope is greatest.

Offline processing of the entire retained record, including the partial cycles at both ends, gives an MAE of 0.3046 mm, an RMSE of 0.5287 mm, and a maximum absolute error of 3.8207 mm. Averaged over the three complete cycles, the MAE and RMSE are 0.2358 mm and 0.2781 mm, respectively; the largest cycle-level absolute error is 1.3780 mm. The 3.8207 mm sample lies outside the complete-cycle subset, but the available log does not establish its physical cause; it is therefore not attributed solely to the partial-cycle endpoints. The measured peak displacement remains within the ±5.5 mm reference amplitude.



(a) experimental test bench **(b) experimental equipment**

Figure 20. Electro-hydraulic valve test bench used for tracking evaluation under nominal operating conditions: (**a**) experimental hydraulic test bench and (**b**) host-computer and data-acquisition equipment.

Table 22. Measurement and communication specifications used in the bench test and offline identification records.

Channel	Sensor or Range	Nominal Resolution/Accuracy
Pilot spool (x_p)	TE MHR100 short-stroke LVDT, ±2.54 mm full range; controller-limited working range of ±2.0 mm	Linearity ±0.25% of full scale; recorded resolution of 0.01 mm.
Main spool (x_m)	TE MHR500 LVDT, ±12.7 mm full range	Linearity ±0.25% of full scale; recorded resolution of 0.01 mm.
Pressure	0–400 bar transducers	Accuracy class 0.25% of full scale.
Flow	1–450 L/min flowmeter range	Flow-meter calibration accuracy was unavailable; it was not reported or propagated into the tracking metrics.
Controller–host logging	CAN link through the CAN analyzer	Nominal platform logging rate of 1 kHz; analyzed feedback aligned to 4 ms (250 Hz).

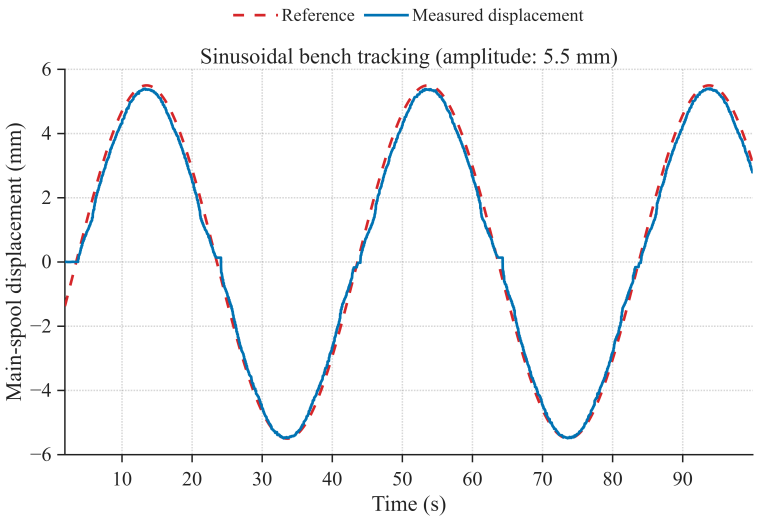


Figure 21. First 100 s of the sinusoidal bench tracking record under nominal operating conditions. Aggregate metrics are evaluated over the entire retained record, while complete-cycle metrics exclude the partial cycles at both ends.

6. Discussion

Separating command-level PWM hysteresis from pilot-opening modes avoids treating the onset thresholds measured in the triangular sweep as PWA switching surfaces. The broader residuals in the active-opening modes indicate that pressure build-up, saturation transitions, and directional friction are represented in lumped form. The predictor is assessed using reset-horizon and mode-conditioned errors, in addition to one-step fitting. The error growth at 120 ms also supports the use of the shorter 80 ms prediction horizon, together with forced refreshes within that horizon.

The lower RMSE of K-DCS-ET-MPC relative to full-rate K-DCS-MPC may reflect retained-plan reuse and pilot-reference smoothing, both of which can reduce unnecessary switching and command chatter. This interpretation is consistent with the controller structure but is not presented as an independently isolated causal effect.

The method is intended for PWM-driven pilot-operated proportional directional valves with main-spool feedback and either pilot-spool feedback or a reliable opening estimate. Application to another valve requires re-identification of the overlap and branch gains, together with recalibration of the pilot servo, stroke limits, and protection bounds. Pressure-control valves require different state and mode definitions.

The robustness and controller-comparison results are based on simulations. Host-side replay measures only the finite-set search routine, and the bench test supports nominal tracking without synchronized search counts, target-MCU timing, or processor-utilization data. Controlled hardware perturbation tests and synchronized embedded timing measurements are therefore still required.

7. Conclusions

A compact pilot-opening-scheduled PWA predictor and a solver-free K-DCS-ET-MPC controller were developed for a PWM-driven electro-hydraulic valve. The guarded validation rule retained the warm-start predictor after reset-horizon evaluation.

In the 20 s simulation, the proposed controller reduced the number of complete finite-set searches by 79.5% relative to TT-MPC. Over the common 5–10 s comparison interval, it achieved the lowest MAE and RMSE among nine controllers while performing 70.18% fewer searches than full-rate K-DCS-MPC. Linear FS-MPC produced the smallest maximum absolute error. The nominal bench test with a sinusoidal reference of 5.5 mm amplitude provided evidence of valve-level tracking; the robustness assessment and controller rankings remain based on simulations.

For the nominal bench test, the entire retained record and the subset containing three complete cycles were evaluated separately. For the entire record, the MAE, RMSE, and maximum absolute error were 0.3046 mm, 0.5287 mm, and 3.8207 mm, respectively. For the complete-cycle subset, the mean MAE and RMSE were 0.2358 mm and 0.2781 mm, respectively, and the largest cycle-level absolute error was 1.3780 mm. The full-record maximum-error sample occurred outside the complete-cycle subset, but its physical cause could not be established from the available log.

Among the tested perturbations, the friction/dead-zone variation produced the largest tracking-error increase. Substantial changes caused by valve wear, oil-temperature variation, contamination, or operating conditions may therefore require recalibration or re-identification of the overlap- and friction-related parameters.

Transfer to another valve or operating range requires re-identification of the pilot overlap and branch gains, together with recalibration of the servo map and protection bounds.

Author Contributions: Conceptualization, J.P.; methodology, J.P.; software, J.P.; validation, J.P. and H.G.; formal analysis, J.P.; investigation, J.P., H.G., H.C. and B.L.; data curation, J.P.; writing—original

draft preparation, J.P.; writing—review and editing, B.S.; visualization, J.P.; supervision, B.S.; project administration, B.S. All authors have read and agreed to the submitted version of the manuscript.

Funding: This research was funded by the National Natural Science Foundation of China (grant number 51875035).

Institutional Review Board Statement: Not applicable.

Informed Consent Statement: Not applicable.

Data Availability Statement: The original contributions presented in the study are included in the article; further inquiries can be directed to the corresponding author.

Acknowledgments: The authors thank the laboratory members for their assistance with the experimental setup and data collection.

Conflicts of Interest: The authors declare no conflicts of interest.

References

1. Ko, Y.-R.; Kim, T.-H. Feedforward plus feedback control of an electro-hydraulic valve system using a proportional control valve. *Actuators* **2020**, *9*, 45. [CrossRef]
2. Li, S.; Du, J.; Shi, Z.; Xu, K.; Shi, W. Characteristics analysis of the pilot-operated proportional directional valve by experimental and numerical investigation. *Energies* **2022**, *15*, 9418. [CrossRef]
3. Yang, M.; Lian, K.; Luo, S.; Yu, C. Simulation analysis and optimization of pilot type electro-hydraulic proportional directional valve based on multi field coupling. *Flow Meas. Instrum.* **2024**, *100*, 102726. [CrossRef]
4. Dai, J.; Xu, H.; Si, L.; Wei, D.; Gu, J.; Chen, H. Research on feedforward-feedback composite anti-disturbance control of electro-hydraulic proportional system based on dead zone compensation. *Machines* **2024**, *12*, 855. [CrossRef]
5. Guo, Y.; Meng, Y.; Peng, X.; Zhou, W. Research on dead zone compensation adaptive control of electro-hydraulic proportional position servo control systems. In Proceedings of the 44th Chinese Control Conference, Chongqing, China, 28–30 July 2025; pp. 2608–2613. [CrossRef]
6. Shi, B.; Xiong, L.; Yu, Z. Pressure estimation of the electro-hydraulic brake system based on signal fusion. *Actuators* **2021**, *10*, 240. [CrossRef]
7. Bertolino, A.C.; De Martin, A.; Jacazio, G.; Sorli, M. A case study on the detection and prognosis of internal leakages in electro-hydraulic flight control actuators. *Actuators* **2021**, *10*, 215. [CrossRef]
8. Shi, Q.; He, L. A model predictive control approach for electro-hydraulic braking by wire. *IEEE Trans. Ind. Inform.* **2023**, *19*, 1380–1388. [CrossRef]
9. Glück, T.; Lobe, A.; Trachte, A.; Bitzer, M.; Kemmetmüller, W. Hybrid control of hydraulic directional valves: Integrating physics-based and data-driven models for enhanced accuracy and efficiency. *ISA Trans.* **2025**, *157*, 280–292. [CrossRef] [PubMed]
10. Ding, Z.; Sun, S.; Zhu, H.; Yan, Z.; Zhou, Y. Learning-enhanced predictive control and experimental validation of an electro-hydraulic track tensioning system for tracked vehicles. *Actuators* **2026**, *15*, 292. [CrossRef]
11. Xu, B.; Shen, J.; Liu, S.; Su, Q.; Zhang, J. Research and development of electro-hydraulic control valves oriented to Industry 4.0: A review. *Chin. J. Mech. Eng.* **2020**, *33*, 29. [CrossRef]
12. Tamburrano, P.; Plummer, A.R.; Distaso, E.; Amirante, R. A review of direct drive proportional electrohydraulic spool valves: Industrial state-of-the-art and research advancements. *J. Dyn. Syst. Meas. Control* **2019**, *141*, 020801. [CrossRef]
13. Li, Y.; Li, R.; Yang, J.; Xu, J.; Yu, X. Recent advances in control strategies and algorithms for pilot-operated electro-hydraulic proportional directional valves. *Proc. Inst. Mech. Eng. Part E J. Process Mech. Eng.* **2025**, *239*, 3881–3902. [CrossRef]
14. Xu, B.; Su, Q.; Zhang, J.; Lu, Z. Analysis and compensation for the cascade dead-zones in the proportional control valve. *ISA Trans.* **2017**, *66*, 393–403. [CrossRef] [PubMed]
15. Zhang, J.; Lu, Z.; Xu, B.; Su, Q. Investigation on the dynamic characteristics and control accuracy of a novel proportional directional valve with independently controlled pilot stage. *ISA Trans.* **2019**, *93*, 218–230. [CrossRef] [PubMed]
16. Lu, Z.; Zhang, J.; Xu, B.; Wang, D.; Su, Q.; Qian, J.; Yang, G.; Pan, M. Deadzone compensation control based on detection of micro flow rate in pilot stage of proportional directional valve. *ISA Trans.* **2019**, *94*, 234–245. [CrossRef] [PubMed]
17. Rout, R.; Kumawat, A.K. Reinforcement learning-based position tracking control for proportional directional control valve-based electro-hydraulic system. *IEEE Access* **2025**, *13*, 159597–159609. [CrossRef]
18. Li, Y.; Li, R.; Yang, J.; Hu, J. Error-enhanced adaptive disturbance rejection control for high-frequency response pilot-operated electro-hydraulic proportional directional valve. *Flow Meas. Instrum.* **2026**, *108*, 103159. [CrossRef]

19. Ma, D.; Zhou, B. Data-driven multi-step nonlinear model predictive control for industrial heavy load hydraulic robot. *arXiv* **2024**, arXiv:2411.13859. Available online: https://arxiv.org/abs/2411.13859 (accessed on 22 June 2026).
20. Bolderman, M.; Lazar, M.; Butler, H. Data-driven feedforward control design for nonlinear systems: A control-oriented system identification approach. In Proceedings of the 62nd IEEE Conference on Decision and Control, Singapore, 13–15 December 2023; pp. 4530–4535. [CrossRef]
21. Bao, Y.; Velni, J.M. Data-driven linear parameter-varying model identification using transfer learning. *IEEE Control Syst. Lett.* **2021**, *5*, 1579–1584. [CrossRef]
22. Breschi, V.; Mejari, M. Shrinkage strategies for structure selection and identification of piecewise affine models. In Proceedings of the 59th IEEE Conference on Decision and Control, Jeju, Republic of Korea, 14–18 December 2020; pp. 1626–1631. [CrossRef]
23. Smarra, F.; Jain, A.; Mangharam, R.; D'Innocenzo, A. Data-driven switched affine modeling for model predictive control. *IFAC-PapersOnLine* **2018**, *51*, 199–204. [CrossRef]
24. Hong, J.; Ramirez-Mendoza, R.A. Zonotope parameter identification for piecewise affine system. *Syst. Sci. Control Eng.* **2020**, *8*, 232–240. [CrossRef]
25. Xu, J. Lattice piecewise affine approximation of explicit linear model predictive control. In Proceedings of the 60th IEEE Conference on Decision and Control, Austin, TX, USA, 14–17 December 2021; pp. 2545–2550. [CrossRef]
26. Augustine, M.T.; Patil, D.U. A practically stabilizing model predictive control scheme for switched affine systems. *IEEE Control Syst. Lett.* **2023**, *7*, 625–630. [CrossRef]
27. Ma, Z.; Lin, X.; Jiang, M.; Tong, M.; Dai, C.; Zhuang, S. Model predictive control of switched piecewise-affine systems under dwell-time constraints. *IEEE Trans. Autom. Control* **2026**, *71*, 3440–3447. [CrossRef]
28. Heybroek, K.; Sjoberg, J. Model predictive control of a hydraulic multichamber actuator: A feasibility study. *IEEE/ASME Trans. Mechatron.* **2018**, *23*, 1393–1403. [CrossRef]
29. Verschueren, R.; Frison, G.; Kouzoupis, D.; van Duijkeren, N.; Zanelli, A.; Novoselnik, B.; Frey, J.; Albin, T.; Quirynen, R.; Diehl, M. Acados: A modular open-source framework for fast embedded optimal control. *Math. Program. Comput.* **2022**, *14*, 147–183. [CrossRef]
30. Ndje, M.; Bitjoka, L.; Boum, A.T.; Fotsa Mbogne, D.J.; Buşoniu, L.; Kamgang, J.C.; Tchané Djogdom, G.V. Fast constrained nonlinear model predictive control for implementation on microcontrollers. *IFAC-PapersOnLine* **2021**, *54*, 19–24. [CrossRef]
31. Nguyen, K.; Schoedel, S.; Alavilli, A.; Plancher, B.; Manchester, Z. TinyMPC: Model-predictive control on resource-constrained microcontrollers. In Proceedings of the IEEE International Conference on Robotics and Automation, Yokohama, Japan, 13–17 May 2024; pp. 1–7. [CrossRef]
32. Liu, C.; Li, H.; Shi, Y.; Xu, D. Distributed event-triggered model predictive control of coupled nonlinear systems. *SIAM J. Control Optim.* **2020**, *58*, 714–734. [CrossRef]
33. Li, P.; Wang, T.; Kang, Y.; Zhao, Y.-B. Event-triggered adaptive horizon model predictive control for perturbed nonlinear systems. In Proceedings of the 59th IEEE Conference on Decision and Control, Jeju, Republic of Korea, 14–18 December 2020; pp. 2392–2397. [CrossRef]
34. Sun, Q.; Chen, J.; Shi, Y. Integral-type event-triggered model predictive control of nonlinear systems with additive disturbance. *IEEE Trans. Cybern.* **2021**, *51*, 5921–5929. [CrossRef] [PubMed]
35. Yang, Y.; Yao, X.; Xu, H. Disturbance-observer-based event-triggered model predictive control of nonlinear input-affine systems. *Automatica* **2024**, *161*, 111504. [CrossRef]

Disclaimer/Publisher's Note: The statements, opinions and data contained in all publications are solely those of the individual author(s) and contributor(s) and not of MDPI and/or the editor(s). MDPI and/or the editor(s) disclaim responsibility for any injury to people or property resulting from any ideas, methods, instructions or products referred to in the content.